Research Square

Preprints are preliminary reports that have not undergone peer review.
They should not be considered conclusive, used to inform clinical practice,
or referenced by the media as validated information.

Djamilar-Induced Localization and the Quantum-Classical Transition

ANISSE ZEROUTA

a.zerouta@precogtec.com

Precog Technologies– Theoretical Physics Division https://orcid.org/0000-0001-7966-0746

Research Article

Keywords: Djamilars, geometric filtration, quantum-classical transition, spontaneous localization, collapse models, matter-wave interferometry, force noise

Posted Date: September 28th, 2026

DOI: https://doi.org/10.21203/rs.3.rs-11162349/v1

License: This work is licensed under a Creative Commons Attribution 4.0 International License.
Read Full License

Additional Declarations: The authors declare no competing interests.

Djamilar-Induced Localization and the Quantum-Classical Transition

From microscopic spacetime apertures to classical matter: mechanism, predictions and experimental opportunities

Anisse Zerouta
Theoretical Physics Division, Precog Technologies
Paris, France
a.zerouta@precogtec.com

Abstract

We propose that the emergence of classical matter is governed by its collective coupling to microscopic spacetime apertures, the Djamilars. A bound domain's mass and physical size activate localization, while the aperture determines how spatial alternatives are resolved. From a completely positive effective dynamics we derive a unique coherence boundary for positive mass amplification at fixed exposure, exact momentum diffusion and heating, and a localization-motion interval in which strong coherence suppression coexists with small positional fluctuations. Size and separation scans reconstruct two lengths whose equality tests the common-aperture identification. A further prediction connects large-separation decoherence to mechanical diffusion: at a fixed geometric state their ratio reconstructs the same aperture for every domain size. For homogeneous spheres in mass-proportional CSL, the corresponding reconstructed length instead grows as the square root of the body radius above the noise correlation length; an exact finite-radius calculation specifies the crossover. This comparison eliminates the overall rate amplitudes. For the Djamilar benchmark, the bare-rate size slope changes from seven to three, while symmetric first-order Talbot attenuation changes from ten to six. Under the stated rigid-domain, independent-force and white-noise assumptions, LISA Pathfinder sets a central normalization ceiling of $2.724\times10^{-4}\,\mathrm{s}^{-1}$. At that ceiling, a specified sodium-cluster geometry reaches unit attenuation at 18.3 nm diameter. These linked predictions develop the quantum-classical sector of the broader DJAMILAR programme: a common geometric account of gravitation, classical matter and dark-sector phenomenology. The effective theory supplies an explicit mechanism and a coordinated experimental programme for investigating that common origin.

Keywords: Djamilars; geometric filtration; quantum-classical transition; spontaneous localization; collapse models; matter-wave interferometry; force noise.

1. A geometric origin for the quantum-classical transition

Why can matter propagate coherently along distinct paths and also form macroscopic bodies with approximately classical trajectories? The Djamilar proposal places the answer in the interaction between matter and the microscopic organization of spacetime. As constituents form a bound material domain, their collective coupling activates a localization process. Its mass and size dependence permits weak localization at microscopic scales and strong suppression of spatial alternatives for larger domains. The objective is to explain the emergence of classical behaviour through a common physical dynamics across these scales.

This objective belongs to a broader founding ambition: a common geometric structure underlying gravitational response, the quantum-classical transition and the galactic and cosmological phenomena usually assigned to a dark sector [1,2]. Djamilars are the proposed microscopic apertures of that structure. Their collective state provides the common variable through which its different physical manifestations are to be related. This article develops the quantum-classical sector as an effective theory, connecting the geometric proposal to a calculable localization mechanism and a concrete experimental programme.

The central proposition is that **mechanical composition and geometric activation together determine the survival of a body's spatial coherence**. Three scales organize the mechanism: the physical size of the material domain, the separation between the alternatives being probed, and the aperture that resolves them. A small molecule can occupy a superposition extending far beyond its own diameter; a large object can be probed over a small displacement. Keeping these scales distinct turns the geometric idea into a quantitative description of when a specified coherence survives.

The emergence of classical behaviour has a substantial theoretical history. Environmental decoherence explains how entanglement with unobserved degrees of freedom suppresses accessible interference [3-5]. GRW and continuous spontaneous localization (CSL) introduce intrinsic stochastic dynamics [6-9], while the Diósi and Penrose proposals investigate a gravitational origin for state reduction [10,11]. DJAMILAR places a geometric activation law within this landscape and seeks a common physical origin for its localization and gravitational sectors. Its contribution is specified by the aperture interpretation, collective-domain rule and linked observables derived below.

Matter-wave experiments supply a route from fullerenes [12] to large organic molecules [13,14], molecules beyond 25 kDa [15], native polypeptides [16] and metal clusters [17]. These systems combine extended material structure with observable quantum propagation. Collisional and thermal-radiation decoherence have themselves been measured in molecular interference [18,19], with the interferometric transfer and thermal protocol dependence developed theoretically [20,21]. The Djamilar mechanism predicts a coordinated pattern across coherence, size and mechanical noise. Interferometry probes how spatial alternatives are resolved; precision mechanics probes the momentum transfer produced by the same channel. Together they can investigate an intrinsic geometric contribution alongside these conventional mechanisms.

Five results give this proposal its quantitative content. We derive the size-dependent coherence boundary; identify two observable length reconstructions that the common-aperture hypothesis requires to agree; link attenuation to momentum diffusion without an independent heating parameter; obtain a size-independent ratio of saturation to curvature at a fixed aperture; and determine the rate interval compatible with both localization and quiet motion. For the reference exponents, collective activation produces a bare-rate size slope of $7 \to 3$. A symmetric first-order Talbot scan instead gives $10 \to 6$ because its exposure grows with mass. These distinct signatures specify what an experiment should extract from its measured signal.

The Gaussian localization generator and its stochastic constructions are established ingredients

[6,22-24]. The Djamilar proposal combines them with a geometric aperture, a collective activation law, a bound-domain prescription and a shared geometric state. Its distinctive physical programme lies in this conjunction: the same proposed spacetime structure is to determine which material domains localize, how spatial alternatives are resolved, and how the associated fluctuations relate to gravitational response. At a fixed aperture, collective activation changes the frequency of events while their momentum-transfer distribution retains its width. In mass-proportional CSL, the body's mass-density form factor also changes that distribution [25,26]. Section 6.5 turns this physical distinction into a comparison of measured quantities. The derivations proceed from these explicit postulates to coherence suppression, effective classical motion under stated scale conditions, and a compatible individual-event construction. The interpretation of those events as physical Djamilar processes is developed as a separate completion question in Section 5.3.

The experimental opportunity is to reconstruct a common geometric scale from several observables. Section 8 sets out the corresponding measurements and a sodium-cluster design target; Section 9 shows how rapid localization and small added motion coexist in a worked example. Section 10 connects this mechanism to the common-origin programme. The assumptions and status of the results are collected in Appendix G.

2. From geometric apertures to a localization law

2.1 Geometric state and the aperture bridge

Let $r_d > 0$ denote an effective Djamilar aperture radius and n_d a proper surface density on a specified microscopic cross-section. The circular-aperture realization defines a dimensionless loading

$$C_d = \pi n_d r_d^2, \qquad \vartheta = \ln \frac{C_d}{C_{d,\mathrm{ref}}}. \tag{1}$$

At fixed density, this gives

$$r_d = r_{d,\mathrm{ref}} e^{\vartheta/2}. \tag{2}$$

If density changes, the exact replacement is

$$\Delta \ln r_d = \frac{1}{2}(\Delta\vartheta - \Delta \ln n_d). \tag{3}$$

Equation (2) follows from the geometry of (1). The effective theory identifies the aperture with the spatial scale of the localization kernel. This identification and the existence of Djamilars are its geometric postulates; the underlying network and continuum construction form the microscopic completion programme discussed in Section 11. The aperture is distinct from an induced-gravity vacuum correlation length or a Planck-scale lattice spacing [2].

We use the terrestrial benchmark $r_d = 25\,\mathrm{nm}$. The independent length reconstructions in Sections 4 and 6 specify how an aperture can be measured. The coherence boundary additionally depends on the object's rate and exposure.

2.2 What constitutes one material domain

The rate law applies to a maximal mechanically bound domain: a connected bound component whose relative coordinates remain sufficiently localized during the protocol, whose fragmentation

or rearrangement does not invalidate a single collective degree of freedom, and whose centre-of-mass coherence is actually probed. Write its mass as M and its physical radius as R. For a spherical body of density ρ_m, $M = c_\rho R^3$ with $c_\rho = 4\pi\rho_m/3$.

The rigid-domain approximation uses $\sigma_{\rm rel} \ll r_d$, where $\sigma_{\rm rel}$ is the instantaneous root-mean-square relative-coordinate fluctuation, together with stability against accumulated diffusion, rearrangement and fragmentation over the protocol. For non-spherical objects, the radius convention and shape response are specified independently of the localization fit.

A dilute cloud or a Bose-Einstein condensate is not automatically one rigid localization domain. For a per-atom interference observable, the domain is the atom unless an independently established collective rigid mode is the observable. Conversely, treating a centimetre-scale solid as one domain is a substantive extrapolation, tested here by LISA Pathfinder.

Each calculation follows a fixed domain with specified M and R. Domain merger, dissociation and superpositions of internal structures belong to the many-body completion. In particular, the linear complete-positivity proof below assumes fixed domain parameters rather than a state-dependent selection from expectation values.

2.3 Size activation and collective amplification

We postulate

$$\Gamma_D = \gamma_0 \left(\frac{M}{m_0}\right)^{\alpha} \mathcal{F}_p(R/r_d), \qquad \mathcal{F}_p(z) = \frac{z^p}{1+z^p}, \quad p > 0, \tag{4}$$

where m_0 is the atomic mass unit and $\gamma_0 \geq 0$ has units of inverse time. The effective exponents α and p specify mass amplification and the activation crossover. We use the benchmark $\alpha = 1$, $p = 4$ for numerical comparisons; the unique-boundary theorem assumes $\alpha > 0$.

For $R \ll r_d$, activation suppresses the rate by $(R/r_d)^p$. For $R \gg r_d$, activation saturates while mass amplification remains. The resulting continuous crossover is the mechanism by which one dynamics can preserve microscopic coherence and strongly localize larger material domains.

3. Dynamics: from one geometric event to decoherence and noise

3.1 A normalized completely positive channel

In a homogeneous patch with fixed r_d and Γ_D, introduce the normalized momentum-transfer density

$$\mu_{r_d}(\mathbf{q}) = \frac{r_d^3}{\pi^{3/2}\hbar^3} e^{-r_d^2 q^2/\hbar^2}, \qquad \int d^3q\, \mu_{r_d}(\mathbf{q}) = 1. \tag{5}$$

For the centre-of-mass position operator $\widehat{\mathbf{X}}$,

$$\dot\rho = -\frac{i}{\hbar}[H,\rho] + \mathcal{L}_D\rho, \qquad \mathcal{L}_D\rho = \Gamma_D \int d^3q\, \mu_{r_d}(\mathbf{q}) \left(e^{i\mathbf{q}\cdot\widehat{\mathbf{X}}/\hbar}\rho e^{-i\mathbf{q}\cdot\widehat{\mathbf{X}}/\hbar} - \rho\right). \tag{6}$$

For a fixed domain this is a trace-preserving, completely positive Markovian localization generator [22,23], belonging to the translation-covariant class characterized by Holevo [27]. Its momentum-transfer and compound-Poisson realization follows the established connection between spatial decoherence and Lévy processes [28]. The rigid-body CSL centre-of-mass dynamics also admits a momentum-transfer representation, with a Gaussian noise filter multiplied by the mass-density

form factor [25,26]. For an extended body that product is generally non-Gaussian. Appendix B gives a direct Poisson-channel proof for (6) that does not depend on a finite-dimensional truncation. The full evolution also requires a well-defined Hamiltonian evolution on the states considered. The localization term is isotropic and conserves mean momentum in the absence of an external force. Its spatial action follows by Gaussian integration:

$$\dot{\rho}(\mathbf{x},\mathbf{x}')\big|_D = -\Gamma_D K(|\mathbf{x}-\mathbf{x}'|;r_d)\rho(\mathbf{x},\mathbf{x}'), \qquad K(d;r_d) = 1 - e^{-d^2/(4r_d^2)}. \tag{7}$$

The probability density is unchanged directly by this term. Short-separation coherence is weakly affected; large-separation coherence decays at Γ_D. The radius R in (4) activates the channel, whereas the separation d in (7) determines how well the channel resolves a particular pair of alternatives.

An effective event picture makes the mechanism explicit. A single event multiplies the off-diagonal element by $\nu(d) = e^{-d^2/(4r_d^2)}$. For independent Poisson events with mean number $\Gamma_D T$,

$$\sum_{n=0}^{\infty} e^{-\Gamma_D T}\frac{(\Gamma_D T)^n}{n!}\nu(d)^n = e^{-\Gamma_D T[1-\nu(d)]}. \tag{8}$$

Weak activation allows coherence to persist; sufficiently frequent resolving events suppress it. Poisson statistics and Gaussian resolution provide the explicit effective realization used throughout this article.

3.2 The mechanical cost of localization

The exact second moment of (5) is

$$\langle q_i q_j\rangle_\mu = \frac{\hbar^2}{2r_d^2}\delta_{ij}. \tag{9}$$

Consequently,

$$\left.\frac{d\langle P_i P_j\rangle}{dt}\right|_D = D_C\delta_{ij}, \qquad D_C = \frac{\hbar^2\Gamma_D}{2r_d^2}. \tag{10}$$

Our one-axis white-force convention is $\langle F_i(t)F_j(t')\rangle = D_C\delta_{ij}\delta(t-t')$. The momentum-diffusion coefficient in a Fokker-Planck equation is $D_{pp} = D_C/2$, and the one-sided force power spectral density per hertz is $S_F^{(1)} = 2D_C$. For a free domain,

$$\left.\frac{d\langle E\rangle}{dt}\right|_D = \frac{3D_C}{2M} = \frac{3\hbar^2\Gamma_D}{4Mr_d^2}. \tag{11}$$

These moments are exact consequences of (6); their derivation does not require the small-separation approximation. At fixed density, heating scales as $R^{3\alpha+p-3}$ below the aperture and $R^{3\alpha-3}$ above it. For $\alpha = 1, p = 4$, the total centre-of-mass heating rate grows as R^4 and then saturates.

Equation (11) quantifies the energy supplied to the material domain by this open-system channel. A common gravitational completion must include the compensating energy-momentum exchange with its underlying degrees of freedom.

4. A calculable boundary for spatial coherence

4.1 The quantity that determines coherence survival

For prescribed semiclassical paths separated by $\Delta\mathbf{x}(t)$, define the exposure

$$\mathcal{A}[r_d;\Delta\mathbf{x}] = \int_0^T dt\, K(|\Delta\mathbf{x}(t)|;r_d), \qquad 0 \le \mathcal{A} \le T. \tag{12}$$

For a fixed domain and stationary parameters, its additional attenuation exponent is

$$\mathcal{D}_D = \Gamma_D \mathcal{A}, \qquad \frac{V}{V_0} = e^{-\mathcal{D}_D}. \tag{13}$$

Here V_0 is the independently modelled conventional visibility. Equation (13) applies to a resolved path-pair coherence or an apparatus harmonic with the stated exposure. The complete forward signal includes all relevant harmonics and mass or velocity averaging, as in established interferometric treatments of decoherence and collapse [20,29,30]. Appendix A derives the path-pair factor with Hamiltonian propagation included and specifies its observable reduction.

Choose an operational survival fraction $0 < \varepsilon < 1$ and let $\chi = -\ln\varepsilon$. The coherence boundary is

$$\boxed{\gamma_0 \left(\frac{M}{m_0}\right)^{\alpha} \frac{(R/r_d)^p}{1+(R/r_d)^p}\,\mathcal{A} = \chi.} \tag{14}$$

Equation (14) gives the boundary in physical size, path separation and duration. It combines the aperture geometry with the domain's rate and the experimental protocol. Across it, the specified centre-of-mass coherence passes from survival above ε to suppression below it. Other degrees of freedom retain their own coherence conditions.

4.2 Existence, uniqueness and asymptotic radii

Proposition 1 (size boundary). Fix $\gamma_0 > 0$, $r_d > 0$, $\rho_m > 0$, $p > 0$, $\alpha > 0$ and an exposure $\mathcal{A} > 0$ independent of the size varied. Equation (14) has one and only one positive solution R_c for every $\chi > 0$.

Proof. At fixed density, the rate is continuous, tends to zero as $R \to 0$, and diverges as $R \to \infty$. Its logarithmic derivative is

$$\frac{d\ln\Gamma_D}{d\ln R} = 3\alpha + \frac{p}{1+(R/r_d)^p} > 0. \tag{15}$$

The intermediate-value theorem and strict monotonicity give existence and uniqueness within the fixed-domain effective dynamics.

The limiting solutions are

$$R_c \simeq \left[\frac{\chi r_d^p}{\gamma_0 (c_\rho/m_0)^\alpha \mathcal{A}}\right]^{1/(3\alpha+p)} \qquad (R_c \ll r_d), \tag{16}$$

$$R_c \simeq \left[\frac{\chi}{\gamma_0 (c_\rho/m_0)^\alpha \mathcal{A}}\right]^{1/(3\alpha)} \qquad (R_c \gg r_d). \tag{17}$$

The appropriate regime must be checked after evaluation. If $\alpha = 0$, attenuation saturates at $\gamma_0 \mathcal{A}$ and a finite boundary exists only for $\chi < \gamma_0 \mathcal{A}$. Negative exponents do not generically produce monotonic macroscopic amplification. If $\mathcal{A}$ changes with size, its derivative must be included, as in Section 8.

For a fixed object and constant separation, a finite boundary in separation exists only if $\chi < \Gamma_D T$:

$$d_c = 2r_d \sqrt{-\ln\left(1 - \frac{\chi}{\Gamma_D T}\right)}. \tag{18}$$

At equality the required separation is infinite; above it the desired suppression is inaccessible in that duration. The transition therefore retains explicit temporal and spatial resolution scales at every object size.

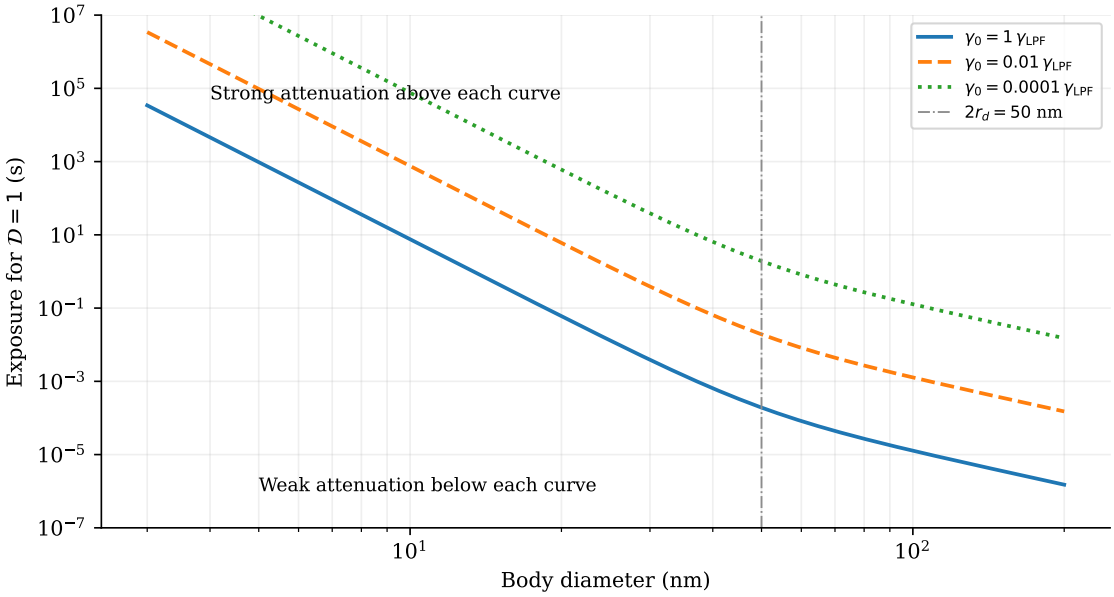


Figure 1: Calculated coherence boundary for spherical sodium domains at constant separation 133 nm, $r_d = 25$ nm, $\alpha = 1$, and $p = 4$. Each curve gives $\mathcal{D}_D = 1$ for a declared normalization. The top curve uses a rate 10^4 times smaller than the LPF central ceiling. The vertical line marks the activation diameter $2r_d$, while the curves give the exposure-dependent coherence boundary.

4.3 A measurable geometric signature

Equation (15) predicts asymptotic rate slopes $3\alpha + p$ and 3α. Their difference is p, independent of γ_0. Moreover,

$$\frac{d^2 \ln \Gamma_D}{d(\ln R)^2} = -\frac{p^2 (R/r_d)^p}{[1 + (R/r_d)^p]^2}. \tag{19}$$

The magnitude of the curvature is maximal at $R = r_d$ and equals $p^2/4$. A resolved, apparatus-corrected rate scan therefore locates the aperture at the crossover and measures p from the slope change. For the benchmark, the bare-rate slopes are $7 \to 3$. These geometric diagnostics eliminate the unknown normalization once a residual channel is resolved over an adequate size range.

5. Collective localization and the emergence of classical motion

5.1 Collective amplification requires collective coupling

Consider N identical constituents of mass m_a and characteristic radius R_a, and a compact aggregate with $R \simeq N^{1/3}R_a$. The single-domain and independent-domain rates obey

$$\frac{\Gamma_{\rm comp}}{\Gamma_{\rm ind}} = N^{\alpha-1}\frac{\mathcal{F}_p(N^{1/3}R_a/r_d)}{\mathcal{F}_p(R_a/r_d)}. \tag{20}$$

If both scales lie below the aperture, the ratio is $N^{\alpha-1+p/3}$. It is $N^{4/3}$ for the reference exponents. If both scales are saturated, it tends to $N^{\alpha-1}$ and equals unity for $\alpha = 1$.

Proposition 2 (independent-constituent restriction). Rigid binding alone does not convert a sum of unchanged, independent constituent momentum-kick generators into the composite activation law (4), except at parameter points where their rates happen to coincide.

Proof. Write $\mathbf{x}_a = \mathbf{X} + \mathbf{r}_a$ with fixed internal coordinates. In a rigid translation, each constituent kick acts on the centre of mass through $e^{i\mathbf{q}\cdot\mathbf{X}/\hbar}$; the fixed internal phase cancels between the two sides of the density operator. Independent generators add, giving $\Gamma_{\rm ind} = N\gamma_0(m_a/m_0)^\alpha\mathcal{F}_p(R_a/r_d)$ for a common kernel. They do not acquire the factor $\mathcal{F}_p(N^{1/3}R_a/r_d)$. Equation (20) states the discrepancy.

The amplification law requires an interaction sensitive to the collective domain, or correlations or coupling changes associated with its formation. Proposition 2 identifies this concrete requirement on the microscopic theory: an unchanged sum of independent constituent couplings supplies a different rate. All comparisons below retain the same domain prescription.

5.2 From the exact dynamics to a classical phase-space equation

For $H = \mathbf{P}^2/(2M) + U(\mathbf{X})$, the exact Wigner-space localization term is

$$\partial_t W|_D = \Gamma_D \int d^3q\, \mu_{r_d}(\mathbf{q})[W(\mathbf{x}, \mathbf{p}-\mathbf{q}) - W(\mathbf{x},\mathbf{p})]. \tag{21}$$

If the momentum dependence varies on scales $P_* \gg \hbar/r_d$, expansion of the convolution gives $D_C\nabla_p^2 W/2$. If the potential varies slowly enough for its Moyal corrections to be negligible, the resulting equation is

$$\partial_t W + \frac{\mathbf{p}}{M}\cdot\nabla_x W - \nabla U\cdot\nabla_p W \simeq \frac{D_C}{2}\nabla_p^2 W. \tag{22}$$

This is the frictionless Kramers equation. Its classical probability interpretation uses three conditions: a controlled momentum-diffusion expansion, negligible potential Moyal corrections, and a positive coarse-grained distribution or negligible Wigner negativity in the observables retained. These are the phase-space and observational qualifications familiar from the decoherence account of classical dynamics [4,5].

The first moments satisfy the exact equations

$$\frac{d\langle\mathbf{X}\rangle}{dt} = \frac{\langle\mathbf{P}\rangle}{M}, \qquad \frac{d\langle\mathbf{P}\rangle}{dt} = -\langle\nabla U\rangle. \tag{23}$$

For a sufficiently narrow distribution in a smooth force field, $\langle \nabla U \rangle \simeq \nabla U(\langle \mathbf{X} \rangle)$ recovers the Newtonian mean-motion equation. For free motion and constant parameters, the added one-axis variances are exactly

$$\Delta \operatorname{Var} P_i = D_C T, \qquad \Delta \operatorname{Var} X_i = \frac{D_C T^3}{3M^2}. \tag{24}$$

These expressions follow by integrating force increments, or directly from the moment hierarchy of (6), without the diffusion truncation. Strong coherence suppression can coexist with small positional wandering because the latter carries the factor M^{-2}. For saturated $\alpha = 1$ domains at fixed r_d, the added position variance scales as $1/M$.

Suppression of the relevant spatial alternatives and small added displacement, together with a suitably prepared distribution and the stated force and phase-space conditions, define the operational regime of approximately classical centre-of-mass motion considered here. Section 9 combines the coherence and added-displacement requirements into an explicit rate interval.

5.3 A compatible individual-event dynamics

Define Gaussian position operators

$$L_{\mathbf{z}} = (\pi r_d^2)^{-3/4} \exp\left[-\frac{(\widehat{\mathbf{X}} - \mathbf{z})^2}{2r_d^2} \right], \qquad \int d^3z \, L_{\mathbf{z}}^\dagger L_{\mathbf{z}} = I. \tag{25}$$

Their integrated channel has the exact matrix elements

$$\left[\int d^3z \, L_{\mathbf{z}} \rho L_{\mathbf{z}}^\dagger \right] (\mathbf{x}, \mathbf{x}') = e^{-|\mathbf{x}-\mathbf{x}'|^2/(4r_d^2)} \rho(\mathbf{x}, \mathbf{x}'). \tag{26}$$

Poisson events of rate Γ_D, with conditional update

$$|\psi\rangle \longmapsto \frac{L_{\mathbf{z}}|\psi\rangle}{\|L_{\mathbf{z}}\psi\|}, \qquad \Pr(d^3z \mid \psi) = \|L_{\mathbf{z}}\psi\|^2 d^3z, \tag{27}$$

therefore reproduce (6) after averaging. This is the established Gaussian localization construction underlying GRW-type dynamics [6,24], here applied to the specified collective rate. Its probability rule is assumed, not derived from geometry. For well-separated narrow branches, an event selects a branch to a good approximation, with weights approaching the squared amplitudes; Gaussian tails remain. Between events, free spreading must also be controlled. A useful comparison is $\tau_{\mathrm{disp}} \sim M r_d^2/\hbar$ against Γ_D^{-1}.

The random momentum kicks in (6) and the position jumps in (27) generate the same density-operator dynamics with different conditional histories. Identifying the position jumps with physical Djamilar events is an additional microscopic postulate; ensemble interference and noise measurements constrain their common channel. The distinction between reduced-state decoherence and an account of individual outcomes is central in the measurement literature [31]. Equations (25)-(27) provide a mathematically compatible route from that channel to individual localized histories, with the displayed probability rule supplied as part of the construction.

6. From geometry to linked experimental predictions

6.1 Measuring the aperture without fixing the rate

For a fixed object at constant separation, define the isolated attenuation rate

$$\mathcal{R}(d) = -\frac{1}{T}\ln\frac{V(d)}{V_0(d)} = \Gamma_D(1 - e^{-d^2/(4r_d^2)}). \tag{28}$$

If both the near-origin curvature and the large-separation saturation are resolved,

$$\mathcal{R}(\infty) = \Gamma_D, \qquad \mathcal{R}''(0) = \frac{\Gamma_D}{2r_d^2}, \qquad \boxed{r_d^2 = \frac{\mathcal{R}(\infty)}{2\mathcal{R}''(0)}}. \tag{29}$$

A scan spanning curvature and saturation determines both the rate and resolving length after accounting for the conventional baseline and path history. If all separations are much smaller than r_d, the leading observable combination is Γ_D/r_d^2; an additional observable or wider separation range resolves the degeneracy.

6.2 One channel linking coherence and mechanical noise

Combining (10) with (29) eliminates the activation law, the mass exponent and the normalization:

$$\boxed{D_C = \hbar^2\mathcal{R}''(0), \qquad S_F^{(1)} = 2\hbar^2\mathcal{R}''(0).} \tag{30}$$

Equivalently,

$$\frac{\mathcal{R}(d)}{D_C} = \frac{2r_d^2}{\hbar^2}(1 - e^{-d^2/(4r_d^2)}). \tag{31}$$

These exact relations predict the mechanical noise associated with an inferred coherence channel, with no independent heating parameter. They hold for the same domain; comparisons between different masses additionally use (4) and the common domain prescription. The curvature identity extends to other symmetric momentum-kick kernels with finite second moment. The Djamilar signature is consequently investigated through the combined activation, resolving length and state dependence, with mechanical noise supplying an independent quantitative measurement of the same coupling.

6.3 A lower mechanical cost of coherence suppression

The coherence-noise relation gives a test even when the aperture is not resolved. Define the squared-separation exposure

$$\mathcal{J}_2 = \int_0^T dt\,|\Delta\mathbf{x}(t)|^2. \tag{32}$$

Proposition 3 (mechanical cost). For the stationary isotropic channel (6), a prescribed path pair with $0 < \mathcal{J}_2 < \infty$ obeys

$$\mathcal{D}_D \le \frac{D_C\mathcal{J}_2}{2\hbar^2}. \quad \text{Hence} \quad \mathcal{D}_D \ge \chi \implies \boxed{D_C \ge \frac{2\hbar^2\chi}{\mathcal{J}_2}}. \tag{33}$$

Proof. The inequality $1 - e^{-u} \le u$ for $u \ge 0$ gives $\mathcal{A} \le \mathcal{I}_2/(4r_d^2)$. Multiplication by Γ_D and substitution of (10) give the result. The Gaussian channel approaches equality when all relevant separations are small compared with r_d.

The bound eliminates γ_0, α, p and r_d. An independently established same-domain ceiling $D_C \le D_{\max}$ therefore rules out the stated localization demand whenever $D_{\max}\mathcal{I}_2 < 2\hbar^2\chi$. Comparing different domains still requires a common coupling law; the LPF momentum diffusion cannot simply be assigned to a cluster.

Appendix F proves the same inequality for every symmetric isotropic momentum-transfer kernel with finite second moment, using $1 - \cos u \le u^2/2$. Within the translation-covariant framework [27,28], this bound is a general consequence of the finite second moment. Its use here connects the geometric activation law to a localization-motion requirement without fitting its four rate and aperture parameters; Appendix F also makes the criterion available for comparing other members of the same class.

6.4 Predictions of the aperture-state identification

Let d_* be the separation at which the dimensionless kernel reaches a fixed value $0 < k_* < 1$:

$$d_* = 2r_d\sqrt{-\ln(1-k_*)}. \tag{34}$$

For two independently specified homogeneous geometric states, constant filtration density and (2) imply

$$\frac{d_{*,2}}{d_{*,1}} = e^{(\vartheta_2-\vartheta_1)/2}, \qquad \frac{(D_C/\Gamma_D)_2}{(D_C/\Gamma_D)_1} = e^{-(\vartheta_2-\vartheta_1)}. \tag{35}$$

The unknown rate cancels even if it changes with state. The comparison uses a geometric-state change specified independently of the visibility data. If n_d varies, the density factors from (3) complete the relation.

The aperture reconstruction and state-ratio relations transfer the common-state architecture [2] into an experimental programme. Determining the absolute normalization γ_0 from the same microscopic structure requires the response-fluctuation matching developed as a completion problem in Section 10.

6.5 A size-dependent comparison with mass-density localization

The body enters the Djamilar generator through the scalar rate (4), while the normalized distribution (5) keeps its width at a fixed aperture. In continuum mass-proportional CSL, the Gaussian noise filter is multiplied by the mass-density form factor $|\tilde{\rho}_m(\mathbf{q})|^2$ [8,25,26]. This changes the relative weights of momentum transfers as the body grows. Coherence and mechanics can distinguish these two prescriptions without fixing either overall rate amplitude.

Let $\Gamma_\infty(R)$ be the large-separation plateau of an isolated localization channel, and let $D(R) = d\,\mathrm{Var}\,P_i/dt$ denote its one-axis momentum-variance production. For the isotropic channels considered here, define

$$r_{\mathrm{eff}}^2(R) \equiv \frac{\hbar^2\Gamma_\infty(R)}{2D(R)}. \qquad \text{DJAMILAR:} \quad r_{\mathrm{eff}}(R) = r_d. \tag{36}$$

The Djamilar equality follows exactly from (10), with $\Gamma_\infty = \Gamma_D$ and $D = D_C$, for a nonzero channel at a common fixed geometric state and aperture. It holds for every fixed domain to which

the declared coupling rule applies, independently of γ_0, α and p. For a non-Gaussian distribution, $r_{\rm eff}$ is a length defined by the ratio of its zeroth and second momentum-transfer moments, rather than a full characterization of the kernel.

For a homogeneous rigid CSL sphere of radius R, with fixed noise correlation length r_C, Appendix H derives the exact finite-radius expression and the limits

$$\text{CSL:} \qquad r_{\rm eff}^2 \longrightarrow r_C^2 \quad (R/r_C \longrightarrow 0), \qquad r_{\rm eff}^2 \simeq \sqrt{\pi}\, R r_C \quad (R \gg r_C). \tag{37}$$

Thus a size scan of the reconstructed length separates a fixed-aperture channel from this specified mass-density channel above its correlation length. The comparison uses the plateau and mechanical response of the same body, or an independently specified transfer between domain assignments. It also requires isolation of the same residual channel from conventional decoherence and force noise. For a large CSL sphere, saturation requires resolving the spatial extent of the mass distribution: $d \gg \max(R, r_C)$ is a sufficient regime. A separation merely exceeding r_C need not reach the plateau. The curvature identity (30) holds for both channels and cannot replace that plateau measurement. The proposed measurement therefore combines size scans, separation scans and mechanical response under a controlled common preparation.

For homogeneous spheres of fixed density, the asymptotic radius slopes of the two observables are

Observable	DJAMILAR, $R \ll r_d$	DJAMILAR, $R \gg r_d$	CSL, $R \ll r_C$	CSL, $R \gg r_C$
Plateau Γ_∞	$3\alpha + p$	3α	6	3
Diffusion D	$3\alpha + p$	3α	6	2

For $\alpha = 1$, $p = 4$, DJAMILAR gives $7 \to 3$ for both quantities. CSL gives $6 \to 3$ for the plateau and $6 \to 2$ for diffusion. At a fixed displacement small compared with r_C, its decoherence rate follows the latter slopes, consistently with its near-origin curvature [25]. An interferometric signal includes the additional apparatus exposure, as Section 8.1 makes explicit. Figure 2 displays the reconstructed length and the bare observable slopes.

CSL also predicts dependence on shape and orientation through the mass distribution [25,32]. A corresponding Djamilar shape test requires an independently specified nonspherical radius and domain rule. The established comparison here concerns spherical size dependence and the two measured moments. A constant $r_{\rm eff}$ would support the fixed-aperture effective law against the stated CSL benchmark; identifying its microscopic origin also uses the independent aperture reconstructions and state relations.

Gravity-related reduction associates localization with the difference between alternative mass distributions [10,11]. Its rate depends on the treatment of short distances and, for a stochastic dynamics, its energy production [33]. Comparisons with that family require a specified regularization and coupling. The fixed-aperture relation (36), the full separation response and the state ratios (35) instead give the geometric proposal its own coordinated set of observables.

7. Experimental anchors and quantitative benchmarks

7.1 The precision-mechanics constraint

LISA Pathfinder measured a residual differential acceleration between two $1.928 \pm 0.001\,\mathrm{kg}$ Au-Pt masses [34-36]. We use the central one-sided amplitude spectral density $1.74\,\mathrm{fm\,s^{-2}}/\sqrt{\mathrm{Hz}}$ in the low-noise band above 2 mHz as a ceiling on an additional white process. The corrected publisher

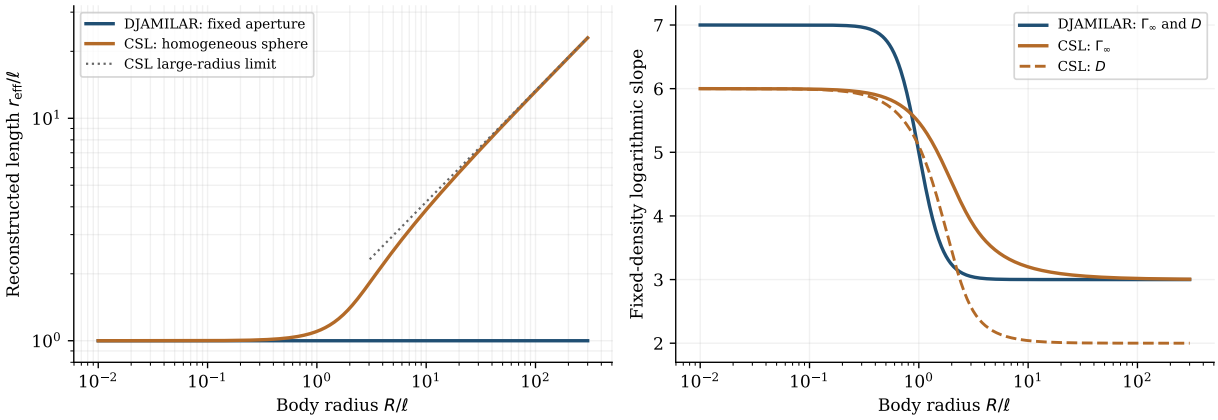


Figure 2: Size dependence of the reconstructed length and of the bare localization observables. Each model uses its own fixed reference length: $\ell = r_d$ for DJAMILAR and $\ell = r_C$ for CSL. Left: the fixed-aperture prediction is compared with the exact homogeneous-sphere CSL result and its large-radius asymptote. Right: fixed-density logarithmic slopes of the decoherence plateau and momentum-variance production; the DJAMILAR curves coincide for the reference exponents. This dimensionless display does not identify the two models' correlation lengths or their rate amplitudes.

abstract gives $\pm 0.05\,\mathrm{fm\,s^{-2}}/\sqrt{\mathrm{Hz}}$; the initially printed ± 0.01 was corrected on 21 February 2018 [34].

If the two forces are independent, the masses equal, and each mass one saturated rigid domain,

$$S_{\Delta g}^{(1)} = \frac{4D_C}{M^2} = \frac{2\hbar^2\gamma_0}{M^2 r_d^2}\left(\frac{M}{m_0}\right)^{\alpha}. \tag{38}$$

The central ceiling is therefore

$$\gamma_{\rm LPF}(r_d,\alpha) = \frac{M^2 r_d^2 S_{\Delta g}^{(1)}}{2\hbar^2}\left(\frac{m_0}{M}\right)^{\alpha}. \tag{39}$$

For $r_d = 25\,\mathrm{nm}$ and $\alpha = 1$,

$$\gamma_0 \lesssim \gamma_{\rm LPF} = 2.724\times 10^{-4}\,\mathrm{s^{-1}}. \tag{40}$$

The propagated relative measurement uncertainty is about 5.75%, corresponding to $1.57\times10^{-5}\,\mathrm{s^{-1}}$ on this central ceiling. This is not a confidence construction for a new signal and excludes the structural uncertainty of the macroscopic domain rule. We subtract no conventional noise contribution.

In general the differential spectrum is $(S_{F_1}+S_{F_2}-2\,\mathrm{Re}\,S_{F_1F_2})/M^2$. Independence is an assumption, not a consequence of trace preservation. The white-noise interpretation also assumes that the same stationary Markovian channel describes both the measured frequency band and the interferometric exposures. A coloured completion would require its own common spectrum. The force-noise methodology follows established collapse-model tests using LISA Pathfinder and gravitational-wave detectors [37,38]; no universal mapping to their parameters is asserted.

7.2 Sodium clusters as a bridge to the transition regime

MUSCLE demonstrates matter-wave interference of sodium clusters in the 143-197 kDa range, centred near 172 kDa [17]. It provides a material system in which physical size, collective binding and quantum propagation can be studied together. We reproduce two count-profile calculations from all 3,895 measurements [39], inserting localization into the first Talbot-Lau harmonic before mass and velocity averaging. Appendix C gives the full statistical model and its convex contrast-phase reduction.

At $r_d = 25\,\mathrm{nm}$, $\alpha = 1$, $p = 4$, and sodium density $971\,\mathrm{kg\,m^{-3}}$, the rounded-velocity profile crosses the conventional criterion $\Delta\chi^2 = 2.71$ at $0.40475\,\mathrm{s^{-1}}$. We retain its rounded value as the numerical diagnostic

$$\gamma_{\mathrm{MUSCLE}}^{\mathrm{diag}} = 0.41\,\mathrm{s^{-1}}. \tag{41}$$

The fixed-normalization binomial fits have substantial absolute lack of fit, with deviances 33,628.4 and 33,471.1 for 3,895 points; the contrast efficiency also reaches its boundary. Accordingly, (41) is a conditional profile diagnostic rather than a validated exclusion or detection. Appendix C documents the residuals, calibration assumptions and coverage issue in full. The independent LPF ceiling (40) supplies the normalization used for the experimental-reach calculations below. The experimental display factor 0.78 is not inserted again into the deposited raw-count likelihood.

The reported internal temperature near 80 K, negligible evaporation and survival over the approximately 12 ms flight support the sodium-domain assignment. Appendix D quantifies the corresponding relative-displacement estimate and states its material assumptions. These observations motivate extending the same material platform toward larger domains and longer controlled exposures.

7.3 Connecting interferometry and precision mechanics

The two observables explore very different mass and activation regimes. At the reference point, the MUSCLE diagnostic normalization is 1.49×10^3 times the LPF central ceiling. Their dependence on aperture and mass amplification connects interferometric design to precision-mechanics measurements. Appendix C records the inherited conditional scaling curves, including the diagnostic crossing near $\alpha = 0.855$.

For the declared domain conventions, the LPF-normalized benchmark gives negligible additional attenuation in the fullerene, Rb and Cs comparisons of Appendix D. These calculations locate a regime that preserves those observed coherences while allowing collective localization to grow with domain size. LUMI is included as a qualitative comparison because its structural radius has not been fixed for this calculation.

8. Experimental opportunities: reconstructing the geometry

The most informative experiment would resolve a linked pattern: a size-dependent activation crossover, a spatial resolving length and the mechanical noise associated with the same channel. The common-aperture hypothesis connects the first two; the coherence-noise identity connects the second and third. These relations give interferometry and precision mechanics complementary roles in investigating one physical mechanism.

This programme builds on complementary interferometric [29,30] and non-interferometric approaches [40]. Ultracold cantilevers probe additional mechanical force noise [41], and layered force sensors exploit the geometry dependence of mass-density coupling [42]. Radiation searches supply another channel, developed for atomic emission [43], underground gravity-related collapse

tests [44] and the Majorana Demonstrator [45]. These studies establish experimental methods and model-specific comparisons. Equations (10)-(11) provide the mechanical translation for the present generator; a radiation prediction additionally requires the electrodynamic coupling described in Appendix G.

The sodium-cluster platform provides a concrete design case. The calculation below identifies the mass, velocity and exposure at which the reference mechanism reaches unit attenuation at the LPF normalization ceiling. The proposed measurements then separate the aperture scale, amplification and overall rate.

8.1 Correct transfer through a Talbot-Lau apparatus

For grating period d_g, the Talbot time is $T_T = Md_g^2/h$. Consider the symmetric, equal-period Talbot-Lau geometry with equal free-flight times $T_s = L/v$ and total duration $T = 2T_s$. In the paraxial regime, with negligible longitudinal momentum redistribution, the ℓth transmitted harmonic has the triangular separation history stated in Appendix A [20]. The grating and propagation approximations are specified by the apparatus; the broader near-field theory includes corrections beyond the eikonal approximation [46]. Its attenuation is

$$R_\ell^D = \exp[-2\Gamma_D T_s f(y_\ell)], \qquad y_\ell = \frac{|\ell| d_g T_s}{\sqrt{2}\, r_d T_T}, \tag{42}$$

$$f(y) = 1 - \sqrt{\frac{\pi}{2}}\frac{\operatorname{erf}(y/\sqrt{2})}{y}, \qquad f(y) = \frac{y^2}{6} - \frac{y^4}{40} + O(y^6). \tag{43}$$

These formulae follow by integrating (7) over that triangular history. Unequal flight times or different grating periods require the appropriate harmonic paths and imaging conditions; they cannot be included by independently replacing the two occurrences of T_s. For a symmetric triangular path with maximum separation $d_{\max}$,

$$K_{\mathrm{tri}} = 1 - \frac{\sqrt{\pi} r_d}{d_{\max}} \operatorname{erf}\left(\frac{d_{\max}}{2r_d}\right), \qquad \mathcal{D}_D = \Gamma_D T K_{\mathrm{tri}}. \tag{44}$$

At symmetric first order, $T_s = T_T$ and $d_{\max} = d_g$ for the first harmonic. At fixed d_g, r_d and density, $T \propto R^3$, so

$$\frac{d\ln \mathcal{D}_D}{d\ln R} = 3\alpha + 3 + \frac{p}{1 + (R/r_d)^p}. \tag{45}$$

The benchmark attenuation slopes are therefore $10 \to 6$. The $7 \to 3$ signature applies to the inferred bare rate or to fixed exposure. An experimental design that confuses these slopes would misidentify the aperture.

8.2 An 18.3 nm first-order design target

For $d_g = 133\,\mathrm{nm}$, segment length $L = 0.98375\,\mathrm{m}$, density $971\,\mathrm{kg\,m^{-3}}$, and the reference parameters, taking $\gamma_0 = \gamma_{\mathrm{LPF}}$ gives $\mathcal{D}_D = 1$ at

$$2R = 18.3\,\mathrm{nm}, \quad M = 1.877\,\mathrm{MDa}, \quad v = 11.82\,\mathrm{m\,s^{-1}}, \quad T = 0.1664\,\mathrm{s}. \tag{46}$$

The uncompensated gravitational drop is 13.57 cm. For diameters 12, 14 and 20 nm, the corresponding exponents are 0.01491, 0.06944 and 2.4116. The complete design table appears in Appendix E.

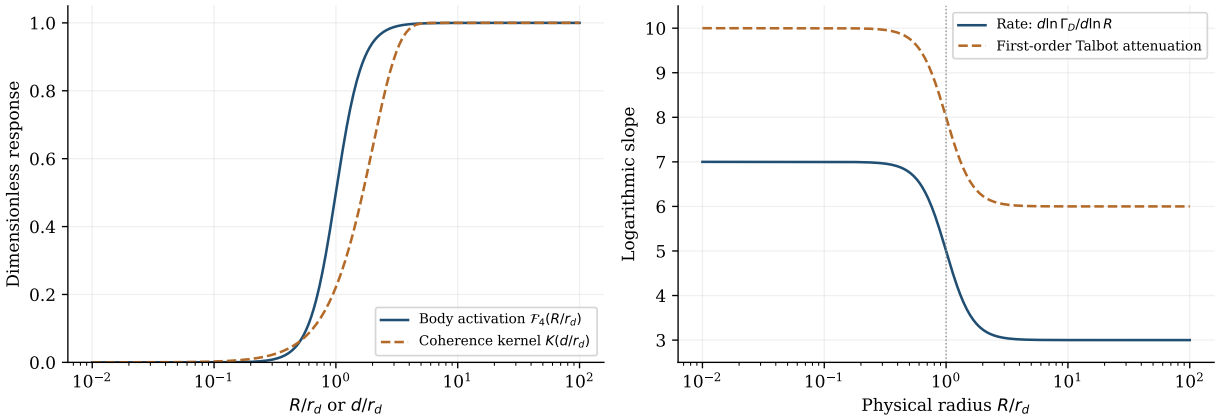


Figure 3: Physical-size activation and path-separation resolution are distinct functions (left). The exact logarithmic slopes of the bare localization rate and first-order Talbot attenuation differ by three at fixed density (right). Parameters: $\alpha = 1$, $p = 4$.

This target corresponds to about eleven times the representative mass of the sodium-cluster dataset. It identifies the earliest unit-attenuation point along the specified first-order scan at the chosen central LPF ceiling; a smaller normalization shifts it to larger sizes. The experiment must resolve quantum propagation through its dependence on apparatus settings, including comparison with classical shadow patterns [17].

At fixed L, d_g, M, operation at Talbot order n gives $v_n = v_1/n$, $T_n = nT_1$, and gravitational drop proportional to n^2. Higher order can increase localization exposure but does not remedy gravitational drop in that fixed geometry. Gravitational compensation, a vertical arrangement, different grating or baseline design, or reduced gravity must be assessed with source flux and conventional decoherence. Reaching the activation crossover itself, $2R = 2r_d = 50$ nm, is substantially more demanding than reaching the conditional 18.3 nm sensitivity point.

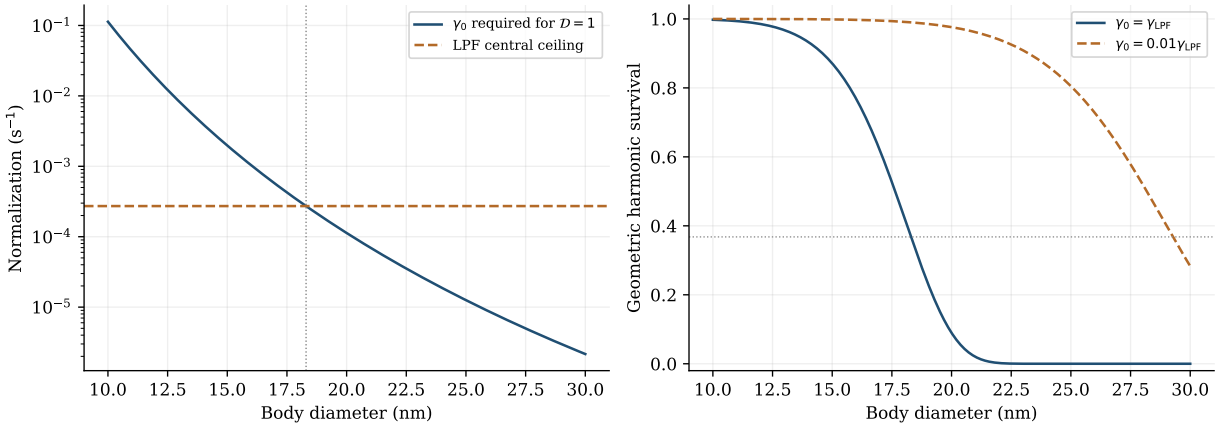


Figure 4: First-order Talbot reach. Left: the normalization required for unit geometric attenuation intersects the central LPF ceiling at 18.3 nm. Right: the resulting geometric harmonic-survival curves differ strongly when the rate is reduced by a factor 100. Conventional visibility losses are not included in these design curves.

8.3 Reconstructing the aperture through linked measurements

Reconstruct the aperture twice. A size scan determines the activation radius from the curvature maximum and the slope change in (15)-(19), after extracting the apparatus exposure.

At selected fixed sizes, a separation scan determines the resolving length from (29). The model predicts equality of the two independently fitted lengths. Observing a common scale through these distinct dependencies would directly support the aperture identification at the level of the effective law. For the reference exponents, the scan targets the bare-rate slopes $7 \to 3$ or the correctly propagated first-order slopes $10 \to 6$.

Measure the mechanical consequence and its size dependence. Once a residual attenuation channel is identified, its near-origin curvature fixes momentum diffusion and force noise through (30). Combining that diffusion with a resolved large-separation plateau reconstructs r_{eff} through (36). Repeating the reconstruction across sizes at a common aperture tests its predicted constancy against the CSL sphere crossover (37). Where experiments use different objects, (4) transfers the Djamilar prediction through their masses, radii and declared domain assignments. Proposition 3 supplies the minimum mechanical cost for a prescribed coherence suppression even when the aperture is unresolved.

Composition, binding and temperature scans provide controlled ways to separate this signature from conventional effects. At fixed radius and geometric state, the rate scales as M^{α}; at fixed mass it follows the activation law. Comparing rigid aggregates with separately localizing constituents probes (20). At fixed state and stable domain, the minimal rate has no explicit temperature dependence, whereas thermal emission changes. These comparisons require independently monitored radius, internal structure and environment; stiffness establishes domain validity rather than supplying an extra fitted rate factor.

The experimental objective is a common pattern across the reconstructed lengths, collective scaling and mechanical response. Its scientific value is to connect the emergence of classical motion to measurable structure in the proposed underlying geometry.

9. Quantitative conditions for the emergence of classical motion

9.1 An explanatory rate floor

A mechanism that accounts for classical motion must suppress specified spatial alternatives on the relevant time scale. For any finite protocol, $\mathcal{D}_D \to 0$ as $\gamma_0 \to 0$; an upper limit alone therefore leaves arbitrarily weak channels available. A declared classicality requirement supplies the complementary lower rate and makes the explanatory objective quantitative. Adler developed lower-rate requirements for CSL by imposing reduction during latent-image formation [47]; more recent work examines the collapse rate needed for classical behaviour [48]. These are requirement-dependent lower bounds. Here the same reasoning yields an explicit rate window for the geometric activation law and a declared spatial-coherence target.

Proposition 4 (operational classicality window). Suppose the mechanism is required to suppress a specified domain's coherence to at most $\varepsilon_{\mathrm{cl}}$ within a declared protocol $(M_{\mathrm{cl}}, R_{\mathrm{cl}}, \mathcal{A}_{\mathrm{cl}})$ with positive exposure. Then

$$\gamma_0 \geq \gamma_{\mathrm{cl}} \equiv \frac{-\ln \varepsilon_{\mathrm{cl}}}{(M_{\mathrm{cl}}/m_0)^{\alpha} \mathcal{F}_p(R_{\mathrm{cl}}/r_d)\mathcal{A}_{\mathrm{cl}}}. \tag{47}$$

If an applicable independent experiment requires $\gamma_0 \leq \gamma_{\max}$, this explanatory realization is possible only if

$$\boxed{\gamma_{\mathrm{cl}} \leq \gamma_{\max}.} \tag{48}$$

Proof. Substitute the required attenuation into (13), solve for the positive normalization, and intersect the resulting half-line with the experimental upper region. Multiple declared classicality

requirements replace the lower limit by their maximum.

The lower rate is defined by a requirement fixed before comparison: a microscopic prediction or an independently justified localization demand. Environmental decoherence contributes its own channel and cannot alone calibrate an intrinsic localization time. With the requirement specified, (47)-(48) give the available rate interval directly.

9.2 Localization with controlled positional fluctuations

An explanation of approximately classical motion must also control its mechanical disturbance. For the same domain, let $\delta_x > 0$ be the allowed root-mean-square displacement *added by this channel* over a duration T. It does not include the prepared wavepacket width or ordinary environmental noise. Write the positive dimensionless amplification as $\mathcal{G} = (M/m_0)^\alpha \mathcal{F}_p(R/r_d)$.

For free motion, (10) and (24) imply

$$\Delta \operatorname{Var} X_i \le \delta_x^2 \quad \Longleftrightarrow \quad \gamma_0 \le \gamma_{\text{quiet}} \equiv \frac{6M^2 r_d^2 \delta_x^2}{\hbar^2 \mathcal{G} T^3}. \tag{49}$$

Consequently, the declared coherence and added-displacement requirements, together with an applicable independent rate ceiling, are simultaneously achievable precisely when

$$\boxed{\gamma_{\text{cl}} \le \gamma_0 \le \min(\gamma_{\max}, \gamma_{\text{quiet}})} \quad \text{has a nonempty interval.} \tag{50}$$

This is the exact feasibility condition for the two operational requirements within the fixed-domain, stationary Gaussian model. Together with the preparation, phase-space and force-smoothness conditions of Section 5, it specifies a regime for approximately classical motion. A force with spatial gradients uses its mechanical response in place of the free variance.

Combining Proposition 3 with the free variance gives the weaker but kernel-independent necessary condition

$$\delta_x^2 \ge \frac{2\hbar^2 \chi T^3}{3M^2 \mathcal{I}_2}. \tag{51}$$

For constant path separation d, this becomes $Md\,\delta_x \ge \hbar T\sqrt{2\chi/3}$. The inequality relates the coherence target to its minimum added motion throughout the stationary kick class of Appendix F.

9.3 A worked example of localization with quiet motion

For illustration, consider a fixed spherical sodium-density domain of radius $1\,\mu$m, separation $1\,\mu$m, exposure 1 ms, and required survival 10^{-6}. With the reference exponents and radius, (47) gives

$$\gamma_{\text{cl}} \simeq 5.64 \times 10^{-9}\,\text{s}^{-1} < \gamma_{\text{LPF}}. \tag{52}$$

Declare, additionally, an allowed added displacement $\delta_x = 1$ nm. Equation (49) gives $\gamma_{\text{quiet}} \simeq 2.28 \times 10^3\,\text{s}^{-1}$, well above the LPF ceiling. Thus the full interval (50) is nonempty. At its localization lower endpoint the added one-axis displacement is 1.57×10^{-15} m; at the LPF ceiling it is 3.46×10^{-13} m. The coexistence of rapid suppression of well-separated alternatives and very small positional noise is mathematically possible within the assumed domain rule.

The worked example establishes a nonempty parameter interval for rapid suppression of the specified coherence with quiet centre-of-mass motion. Its lower rate is fixed by the declared

illustrative requirement; it is not an experimental calibration. This coexistence supplies quiet macroscopic motion over the declared duration, while size activation suppresses the same channel for microscopic domains.

10. One geometric architecture for quantum matter and gravitation

DJAMILAR seeks a common microscopic account of gravitational response and the emergence of classical matter, with galactic and cosmological applications developed in the companion programme [1,2]. The organizing idea is that one structure has both a response, entering gravitation, and fluctuations, entering localization. Equations (1)-(3) and (35) connect the quantum-classical sector to the same geometric state. A state inferred independently through one physical sector would then constrain the characteristic scales of another.

For an initially factorized system and underlying environment, a conditional interaction gives schematically

$$\sum_a c_a|a\rangle|E_0\rangle \longrightarrow \sum_a c_a|a\rangle|E_a(\vartheta)\rangle, \quad \rho_{ab} = c_a c_b^*\langle E_b(\vartheta)|E_a(\vartheta)\rangle. \tag{53}$$

Equation (53) gives the reduced-state construction familiar from environmental decoherence [4,5,31], whose overlap is here to be calculated from Djamilar interactions. Its extension to pairs of system histories is the influence-functional approach of Feynman and Vernon [49]. Equations (4)-(8) specify the proposed effective localization behaviour. The interaction must produce the stated growth of distinguishability with collective activation; this is a microscopic coupling requirement, since reducing a generic coupling can instead preserve coherence.

A common microscopic derivation must match the retarded gravitational response and the localization fluctuation spectrum. Stochastic gravity provides an established framework for distinguishing response and stress-tensor fluctuations [50]. These are distinct quantities, so an induced Einstein coefficient alone does not determine γ_0. A stationary zero-temperature sector with a true excitation gap does not generically supply an unsuppressed white spectrum below that gap; the simplest identification of that vacuum with the required white bath fails in this regime. The common-origin construction must therefore supply the appropriate collective or excited spectrum together with its energy exchange and domain coupling.

The aperture-state relation supplies a conditional cosmological connection. At constant n_d, along the preferred flow,

$$\frac{d\ln\bar{r}_d}{dt} = \frac{\bar{Q}}{2}, \qquad \bar{Q} = Q_0 + \frac{\mathcal{C}_Q}{2K_2a^3} \tag{54}$$

for the quadratic temporal representative $\mathcal{K}(Q) = K_2(Q-Q_0)^2$, $K_2 > 0$, with conserved charge $\mathcal{C}_Q = a^3\mathcal{K}_Q$ [2]. Here a is the homogeneous scale factor, $\mathcal{K}_Q = d\mathcal{K}/dQ$, and $Q = u^\mu\nabla_\mu\vartheta$ for the unit preferred-flow vector u^μ; on the homogeneous background $\bar{Q} = d\bar{\vartheta}/dt$. Natural units are used in (54); if Q is in inverse metres, conversion to a derivative per second supplies a factor c. This is a homogeneous relation within that representative, not a complete cosmological solution. A laboratory derivative is $\frac{1}{2}v^\mu\nabla_\mu\vartheta$ along its unit four-velocity v^μ in the same unit convention, and requires a matched local solution. No nonzero laboratory drift, or force-normalization determination of γ_0, is inferred without that solution.

The stochastic coupling depends on the absolute aperture state at fixed reference radius, whereas a derivative-only classical action has a shift symmetry. Their joint construction must include

backreaction and any induced state-dependent operators. The resulting matching problem gives the common-origin ambition a concrete target: calculate gravitational response, aperture evolution and localization from a shared microscopic state.

11. Discussion and research programme

The effective theory connects a geometric hypothesis to a coherent set of quantitative consequences. Collective activation specifies how the localization rate grows with material size; the spatial kernel specifies how that rate acts on a chosen superposition. Their combination determines the coherence boundary. The same channel fixes diffusion and heating, while the localization-motion interval identifies conditions in which spatial alternatives are suppressed with little added positional wandering. These results describe nonrelativistic fixed domains in homogeneous patches, with the propagation and preparation conditions stated alongside the derivations.

The experimental strength of the proposal lies in the conjunction of its predictions. Size and separation scans reconstruct two lengths. Mechanical measurements determine the noise associated with the resolving kernel. The ratio of decoherence saturation to diffusion should reconstruct a size-independent aperture at a fixed state, while the explicit CSL benchmark has a form-factor crossover. Composition and binding control amplification. A shared geometric state adds relations between independently specified environments. This conjunction permits an investigation of the geometric mechanism through several observables of the same law; the general coherence-noise identities also remain useful for comparing other localization models.

The theoretical priority is a microscopic derivation of the collective coupling, activation and event statistics, including the many-body rule for changing domains. A common gravitational origin further requires the response-fluctuation matching and energy exchange of Section 10. The compatible jump construction specifies the additional event and probability postulates needed for an individual-outcome interpretation. Appendix G collects the technical domain assumptions and the status of each result.

The displayed effective law already supplies a concrete research programme. Experiments can seek its common length and linked mechanical response while microscopic theory develops the geometric construction. This makes the proposed origin of classical behaviour an experimentally addressable question, with a quantitative target for both communities.

12. Conclusion

The Djamilar proposal gives the quantum-classical transition a geometric mechanism: the collective coupling of a bound material domain controls how rapidly the underlying structure resolves its spatial alternatives. Within the effective dynamics developed here, this mechanism yields a calculable coherence boundary and a regime where strong localization coexists with quiet centre-of-mass motion. Mass, physical size, path separation and duration enter one quantitative account.

Its characteristic predictions are linked. The size crossover and separation dependence reconstruct lengths that the common-aperture hypothesis requires to agree. The same channel determines momentum diffusion and heating, providing an independent mechanical measurement of an inferred coherence process. At a fixed geometric state, combining diffusion with the decoherence plateau reconstructs one aperture across body sizes. The exact CSL sphere comparison makes this a quantitative distinction between two specified localization laws, independent of their overall rate amplitudes. The explicit localization-motion interval connects these observables to the explanatory requirement of approximately classical motion.

For the reference parameters and normalization at the stated LPF ceiling, the symmetric first-order sodium-cluster design reaches unit attenuation at 18.3 nm diameter. This conditional target, together with the two aperture reconstructions and the coherence-noise relation, defines a concrete opportunity for matter-wave and precision-mechanics experiments to investigate the proposed geometric scale.

The ambition is a common physical account of classical matter and gravitation rooted in the microscopic structure of spacetime. The present theory develops the quantum-classical part of that programme into explicit dynamics, derived relations and experimental targets. It invites the search for an underlying geometry through the coordinated behaviour of coherence and motion.

Data and code availability

The primary MUSCLE data and Talbot-Lau analysis are deposited by the experiment authors at DOI 10.5281/zenodo.17502163 [39]. The supplementary archive accompanying this manuscript, `DJAMILAR_Quantum_Classical_Supplement.zip`, contains the manuscript sources, figures, analytic verification script and outputs, the retained global recalculation archive, and a portable raw-count reproduction with unchanged source data and source checksums.

The `reproduction/` directory contains the finite-grid nominal and rounded-velocity profiles, complete grid outputs, per-point and per-scan residuals, forward-model checks and optimization diagnostics. These two profiles are recalculated from all raw counts; remaining mass-spectrum alternatives and aperture/exponent scans are inherited and identified as such. Their statistical interpretation is stated in Section 7.2 and Appendix C. The analytic script separately checks the LPF ceiling, boundary and moment calculations, mechanical-cost inequalities and localization-motion window. The additional script `verify_csl_discriminant.py` checks the exact sphere expressions against independent momentum-space quadrature, regenerates the comparison figure and evaluates the per-scan residual decomposition. The README provides reproduction commands and dependencies.

Appendix A. Derivation and validity of the coherence boundary

The localization term (7) is diagonal in the position-pair representation, but Hamiltonian propagation generally mixes those pairs. A time-sliced density-matrix path integral instead assigns each forward and backward path pair the product of factors $\exp[-\Gamma_D K(|\mathbf{x}_k - \mathbf{x}'_k|; r_d)\Delta t]$. In the continuum limit this product is $\exp[-\Gamma_D \mathcal{A}]$ for that pair. Extracting it as a measured attenuation requires a resolved prescribed path pair or the corresponding harmonic reduction of the apparatus, not merely a change to the interaction picture. The geometry must include the full separation history.

For the symmetric equal-period Talbot-Lau geometry, the paraxial harmonic propagation [20] supplies, for $0 \le t \le 2T_s$,

$$d_\ell(t) = \frac{|\ell| d_g}{T_T} \min(t, 2T_s - t). \tag{A1}$$

Its maximum is $|\ell| d_g T_s / T_T$. Integrating the kernel along the two ramps gives (42)-(44). All numerical Talbot calculations here use this symmetric geometry; no asymmetric extension is needed for their quoted values.

For a linear ramp $\Delta x(t) = d_{\max} t/T$, substitution $u = t/T$ gives

$$\frac{\mathcal{A}}{T} = \int_0^1 du\,[1 - e^{-d_{\max}^2 u^2/(4r_d^2)}] = K_{\rm tri}. \tag{A2}$$

A symmetric triangular path has the same average because each half traverses the same ramp. The small-separation limit is $K_{\rm tri} = d_{\max}^2/(12r_d^2) + O(d_{\max}^4/r_d^4)$. This agrees with (43) when $y = d_{\max}/(\sqrt{2}r_d)$.

At fixed exposure and density, differentiation of $\ln\Gamma_D = \ln\gamma_0 + \alpha\ln(c_\rho R^3/m_0) + p\ln(R/r_d) - \ln[1+(R/r_d)^p]$ gives (15) and (19). The curvature magnitude is proportional to $u/(1+u)^2$, which has its unique maximum at $u = 1$. The claims concern the rate, not an uncorrected mass-averaged contrast curve.

More generally the observed exponent slope is

$$\frac{d\ln\mathcal{D}_D}{d\ln R} = 3\alpha + \frac{p}{1+(R/r_d)^p} + \frac{d\ln\mathcal{A}}{d\ln R}. \tag{A3}$$

State changes, density changes and non-spherical geometry introduce additional declared derivatives. The use of the crossover to infer r_d requires those effects to be modelled independently.

Appendix B. Gaussian events, moments and the classical limit

Define the channel $\Phi(\rho) = \int d^3q\,\mu_{r_d}(\mathbf{q})e^{i\mathbf{q}\cdot\widehat{\mathbf{X}}/\hbar}\rho e^{-i\mathbf{q}\cdot\widehat{\mathbf{X}}/\hbar}$. It is a normalized mixture of unitary conjugations. The localization semigroup alone is

$$e^{t\mathcal{L}_D}\rho = e^{-\Gamma_D t}\sum_{n=0}^{\infty}\frac{(\Gamma_D t)^n}{n!}\,\Phi^n(\rho). \tag{B1}$$

Every summand is completely positive and trace-preserving, and the positive weights sum to one. The series converges in trace norm. Alternating this channel with the unitary Hamiltonian evolution gives the full dynamics under the usual existence assumptions. No commutation between the Hamiltonian and localization superoperators is assumed.

Using

$$|\mathbf{x}-\mathbf{z}|^2 + |\mathbf{x}'-\mathbf{z}|^2 = 2\left|\mathbf{z} - \frac{\mathbf{x}+\mathbf{x}'}{2}\right|^2 + \frac{|\mathbf{x}-\mathbf{x}'|^2}{2}, \tag{B2}$$

the Gaussian integral of $L_{\mathbf{z}}(\mathbf{x})L_{\mathbf{z}}(\mathbf{x}')$ equals (26). Normalization follows by setting $\mathbf{x}' = \mathbf{x}$. For an arbitrary state, averaging the norm-weighted update in (27) cancels its denominator and gives the linear integrated channel. Poisson averaging then yields (6). No preferred individual realization follows from that equality of ensemble channels.

The adjoint kick maps P_i to $P_i + q_i$. Odd moments vanish, and the isotropic second moment gives (10). The generator leaves functions of position unchanged instantaneously, so its free moment hierarchy is

$$\frac{d\langle P_i^2\rangle}{dt} = D_C, \quad \frac{d\langle X_iP_i + P_iX_i\rangle}{dt} = \frac{2\langle P_i^2\rangle}{M}, \quad \frac{d\langle X_i^2\rangle}{dt} = \frac{\langle X_iP_i + P_iX_i\rangle}{M}. \tag{B3}$$

Subtracting the Hamiltonian-only solution gives (24). In a force field, (23) remains exact but the free variance formula does not. Classical trajectories are then an approximation with the appropriate force response and noise propagation.

Equation (22) neglects higher momentum derivatives when the kick scale is small relative to the resolved momentum variation. It neglects potential Moyal terms when the corresponding force and state scales suppress them. If either condition fails, the exact quantum jump equation (21) must be used. A positive coarse-grained phase-space distribution and sufficiently small added position noise supply the operational interpretation; the Wigner function need not become pointwise positive merely because one interference pattern is suppressed.

Appendix C. Count-profile results and spectral conventions

C.1 Statistical model and numerical provenance

The MUSCLE count likelihood follows the deposited binomial working model [17,39]. For phase point i, let k_i be the transmitted count and N_i the tabulated incident-count normalization, treated as known. With predicted transmission $\mathcal{T}_i$, mass- and velocity-averaged visibility V_i, and grating phase $\psi_i = 2\pi x_i/d_g$,

$$\begin{aligned} s_i &= \mathcal{T}_i[1 + \eta V_i \cos(\psi_i + \varphi)], \\ \ell &= \sum_i \{k_i \ln s_i + (N_i - k_i)\ln(1 - s_i)\}. \end{aligned} \tag{C1}$$

Terms independent of the model parameters are omitted. The geometric factor in (42) multiplies each mass-velocity component of the first harmonic before averaging. The source mass-spectrum window is $(144.5, 195.5)$ kDa, with 52 interpolated mass nodes and weighted mean 171.284 kDa; 172 kDa is a representative experimental mass, not that exact numerical mean. The velocity integration retains 45 nodes. The source archive checksum agrees with the primary deposit [39].

The archived reproduction of the original macroscopicity calculation [51] returns $\tau_{5\%} = 2.84\times10^{15}\,\mathrm{s}$ and $\mu = 15.45$. That Bayesian analysis is distinct from the geometric-channel profiles and is not recalculated here.

The profile varies global contrast efficiency $\eta \in [0, 1]$, phase $\varphi \in [-\pi, \pi]$, polarizability per atom with the stated Gaussian calibration penalty $4.5 \pm 0.5\,\text{Å}^3$, and a dimensionless ionization scale constrained by transmission. The nominal setting $(\bar{v}, \sigma_v) = (158, 9)\,\mathrm{m\,s^{-1}}$ uses 63 calibration pairs: polarizability 4.70-5.30 in steps of 0.10, and ionization scale 0.960-1.000 in steps of 0.005. The rounded setting $(160, 10)\,\mathrm{m\,s^{-1}}$ uses 40 pairs: polarizability 4.75-5.10 in steps of 0.05, and ionization scale 0.990-1.010 in steps of 0.005. Polarizabilities are in Å^3 per atom.

Both rate grids cover $0 \le \gamma_0 \le 0.45\,\mathrm{s^{-1}}$, with finer sampling near the upper crossings; the supplied script states every node. Subtracting half the squared standardized polarizability deviation gives the penalized log likelihood. At each rate the largest value over its declared calibration grid is retained. The reported $\Delta\chi^2$ is twice its decrease from the largest value over that entire rate grid; crossings are linearly interpolated. This is a finite-grid envelope, not proof of a continuous outer optimum. Other archived velocity and mass-spectrum alternatives are not rerun here. Beam-power and waist errors are not added again as independent Gaussian penalties because the covariance of the inferred photophysical products is unavailable.

The contrast-phase block can be solved with a global error check. Put $\mathbf{z} = (a, b) = (\eta\cos\varphi, -\eta\sin\varphi)$, so $|\mathbf{z}| \le 1$, and $s_i = \mathcal{T}_i + \mathbf{h}_i \cdot \mathbf{z}$ with $\mathbf{h}_i = \mathcal{T}_i V_i(\cos\psi_i, \sin\psi_i)$. For $f = -\ell$ up to a constant,

$$\nabla^2 f = \sum_i \left[\frac{k_i}{s_i^2} + \frac{N_i - k_i}{(1 - s_i)^2} \right] \mathbf{h}_i \mathbf{h}_i^{\mathsf{T}} \succeq 0. \tag{C2}$$

Thus f is convex on the physical disk. All sampled forward models satisfy $0 < \mathcal{T}_i(1 - V_i) \leq s_i \leq \mathcal{T}_i(1 + V_i) < 1$ throughout that disk; no clipping of probabilities is used. If $\mathbf{g} = \nabla f(\mathbf{z})$, convexity gives $f(\mathbf{y}) \geq f(\mathbf{z}) + \mathbf{g} \cdot (\mathbf{y} - \mathbf{z})$. Minimizing the right-hand side over $|\mathbf{y}| \leq 1$ proves

$$0 \leq f(\mathbf{z}) - f_{\min} \leq |\mathbf{g}| + \mathbf{g} \cdot \mathbf{z}. \tag{C3}$$

The computed right-hand side stays below 10^{-8} in log-likelihood units for all 14,293 fitted grid points. This floating-point optimality diagnostic is not interval-arithmetic certification and controls only the inner contrast-phase block. The forward transmission and zero-localization visibility also agree with the deposited Talbot-Lau routine at three test scans to numerical precision; direct integration checks the geometric harmonic exposure. These controls verify reproduction of the chosen model, not its empirical adequacy.

Profile	Crossing at $\Delta\chi^2 = 2.71$	Crossing at $\Delta\chi^2 = 3.84$
Nominal calibration setting	$0.36324\,\mathrm{s}^{-1}$	$0.36684\,\mathrm{s}^{-1}$
Rounded velocity setting $(160, 10)\,\mathrm{m\,s}^{-1}$	$0.40475\,\mathrm{s}^{-1}$	$0.40775\,\mathrm{s}^{-1}$

The contrast-efficiency optimum reaches $\eta = 1$ near $\gamma_0 = 0.353\,\mathrm{s}^{-1}$ for the nominal setting and near $0.390\,\mathrm{s}^{-1}$ for the rounded setting. The subsequent steep rise is boundary-driven. Asymptotic likelihood criteria [52] do not establish coverage when the required regularity and model-adequacy conditions fail. The nominal null comparison $\Delta\chi^2 \simeq 2.03$ is not converted into a detection significance.

To assess absolute fit separately from relative profiling, define the unpenalized saturated deviance and Pearson statistic at the fitted probabilities:

$$\begin{aligned} D_{\mathrm{sat}} &= 2 \sum_i \left[k_i \ln \frac{k_i}{N_i \hat{s}_i} + (N_i - k_i) \ln \frac{N_i - k_i}{N_i (1 - \hat{s}_i)} \right], \\ X_{\mathrm{P}}^2 &= \sum_i \frac{(k_i - N_i \hat{s}_i)^2}{N_i \hat{s}_i (1 - \hat{s}_i)}. \end{aligned} \tag{C4}$$

Setting	D_{sat}	X_{P}^2	$\sqrt{X_{\mathrm{P}}^2/3895}$
Nominal	33,628.4	33,727.4	2.943
Rounded velocity	33,471.1	33,467.2	2.931

These values substantially exceed the count-noise scale of order the number of points; predicted counts exceed 1,500 at every point. The same grid points minimize the raw deviance over the computed grids, so removing the calibration penalty does not remove this discrepancy. No exact goodness-of-fit p-value is assigned. The fixed-normalization independent-binomial working model on these grids is inadequate for interpreting the crossings as validated exclusions. The discrepancy does not identify its cause or demonstrate a failure of the underlying localization law: calibration errors, scan correlations and omitted signal structure require independent assessment. A revised

generative count model can represent normalization fluctuations and correlations when supported by the acquisition and calibration information. Its adequacy must be established before calibrating the coverage of a rate bound. A single overdispersion factor does not establish that adequacy.

The nominal per-scan residuals give a further diagnostic. With $z_{sj} = (k_{sj} - N_{sj}\hat{s}_{sj})/[N_{sj}\hat{s}_{sj}(1 - \hat{s}_{sj})]^{1/2}$, the identity $\sum_{sj} z_{sj}^2 = \sum_s n_s \bar{z}_s^2 + \sum_{sj}(z_{sj} - \bar{z}_s)^2$ separates scan means from within-scan structure. The first term is 17,518.1 out of 33,727.4, or 51.94%; after arithmetic centring within each scan, the root-mean-square residual is 2.040 over the 3,895 points. This decomposition neither refits the probabilities nor identifies a cause. It motivates investigating scan normalization together with within-scan structure rather than attributing the discrepancy to a unique flux fluctuation.

The 0.40475 crossing is used only in conditional algebraic comparisons; 0.41 is its rounded presentation. Radius and mass-exponent scans in the retained global archive use the selected rounded-velocity calibration branch ($v = 160\,\mathrm{m\,s^{-1}}$, $\sigma_v = 10\,\mathrm{m\,s^{-1}}$, polarizability $4.95\,\mathrm{\AA}^3$ per atom and ionization scale 0.995), with contrast and phase profiling. Their reference normalization is anchored to the stated crossing. They are neither a renewed full-calibration profile at every radius and exponent nor validated experimental exclusion curves.

The earlier fixed-calibration result $1.818\times10^{-2}\,\mathrm{s^{-1}}$ is not the final profile scale. The proxy $-\ln(0.9)$ is not an experimental bound. Neither is used to strengthen the localization inference.

C.2 Dependence on the aperture radius

r_d (nm)	MUSCLE diagnostic scale ($\mathrm{s^{-1}}$)	LPF central ceiling ($\mathrm{s^{-1}}$)	Ratio
1	1.81357×10^{-4}	4.35785×10^{-7}	416.16
2	1.93863×10^{-4}	1.74314×10^{-6}	111.21
3	2.38419×10^{-4}	3.92207×10^{-6}	60.79
4	3.54784×10^{-4}	6.97256×10^{-6}	50.88
4.1256	3.77163×10^{-4}	7.41731×10^{-6}	50.85
5	6.01315×10^{-4}	1.08946×10^{-5}	55.19
7	1.82239×10^{-3}	2.13535×10^{-5}	85.34
10	7.37611×10^{-3}	4.35785×10^{-5}	169.26
15	4.06819×10^{-2}	9.80516×10^{-5}	414.90
25	4.04750×10^{-1}	2.72366×10^{-4}	1486.05
50	1.37773×10^{1}	1.08946×10^{-3}	1.2646×10^{4}
100	7.05009×10^{2}	4.35785×10^{-3}	1.6178×10^{5}

These are inherited selected-branch calculations at $\alpha = 1, p = 4$, retained as numerical diagnostics. The tabulated digits facilitate reproduction and are not a precision statement about calibration, statistical adequacy or domain assumptions. The LPF uncertainty correction leaves the central values unchanged.

For sub-aperture bodies with well-resolved path separation, interferometry probes approximately γ_0/r_d^p. If the separation is also much smaller than r_d, the leading combination is instead γ_0/r_d^{p+2}. The saturated LPF limit probes γ_0/r_d^2. Thus γ_0/r_d^p is not a universal interferometric invariant over an unrestricted aperture scan.

C.3 Spectral uncertainty and exponent comparison

With $\langle F(t)F(t')\rangle = D_C\delta(t-t')$, the one-sided PSD is $2D_C$. Two independent equal-mass forces give $4D_C/M^2$. Substituting the saturated rate yields (39) without an additional factor of two.

At $\alpha = 1$, fixed r_d and independent measurement errors,

$$\left(\frac{\sigma_\gamma}{\gamma_{\mathrm{LPF}}}\right)^2 = \left(\frac{\sigma_M}{M}\right)^2 + 4\left(\frac{\sigma_{\mathrm{ASD}}}{\mathrm{ASD}}\right)^2. \tag{C5}$$

Using the corrected 0.05/1.74 ratio gives 5.747%. It does not include uncertainty in r_d or in the spectral and domain assumptions. A chosen confidence ceiling would require an explicit statistical construction for the spectrum and is not obtained by calling the central residual a 95% limit.

For effective masses M_s and M_L, and the reference normalization ratio $Q = 0.40475/\gamma_{\mathrm{LPF}}$, the approximate exponent crossing is

$$\alpha_* \simeq 1 + \frac{\ln Q}{\ln(M_s/M_L)}. \tag{C6}$$

With the representative $M_s = 172{,}000 m_0$ and $M_L = 1.928\,\mathrm{kg}$, this gives 0.854689. The aperture-averaged selected-branch calculation gives 0.854633. Neither value bypasses calibration uncertainty, the mass distribution or the common-domain premise; the crossing remains diagnostic because the MUSCLE statistical model has not passed the adequacy check above.

Appendix D. Material-domain and comparison checks

D.1 Sodium rigidity

The MUSCLE supplementary information places the internal temperature near 80 K and describes thermal evaporation as negligible [17]. With $L = 0.98375\,\mathrm{m}$ and $v = 160\,\mathrm{m\,s^{-1}}$, the first-to-third-grating duration is $2L/v = 12.2969$ ms. The equivalent radii at density $971\,\mathrm{kg\,m^{-3}}$ are 3.87935, 4.12563 and 4.31654 nm for 143, 172 and 197 kDa.

A Debye estimate using the Na^+_{139} comparator temperature $\Theta_D = 163.5 \pm 10$ K [53] gives a three-dimensional single-atom displacement $u_{\mathrm{RMS}} = 0.02513$ nm at 80 K. The uncorrelated-pair comparator is $\sigma_{\mathrm{rel}} = \sqrt{2}u_{\mathrm{RMS}} = 0.03554$ nm, or $1.42 \times 10^{-3} r_d$. A softened comparator $\Theta_D = 100$ K gives 0.05629 nm. These are small instantaneous displacements, not a proof of negligible long-time rearrangement.

Studies of smaller sodium clusters provide thermal comparators [54-57], but are not direct structural measurements of the selected multi-thousand-atom clusters. Survival, temperature and the displacement estimates support the domain rule for the approximately 12 ms protocol under the stated hypothesis. A slower future design must repeat the stability assessment over its own exposure.

D.2 Selected interference checks

Experiment	Domain convention and input	$\mathcal{D}_D$ at the LPF ceiling
C_{60} diffraction [12,58]	One molecule; $R = 0.35325$ nm; 5.682 ms	4.44×10^{-11}
LUMI oligoporphyrins [15]	One molecule; 26,777 Da representative mass; 7.5 ms	Not assigned
^{87}Rb Cold Atom Lab [59]	One atom; 1 ms sequence	1.41×10^{-13}
^{133}Cs fountain [60]	One atom; 320 ms sequence	1.05×10^{-10}

The fullerene radius is half the measured mean atom-to-atom diameter, not an unspecified bulk-volume radius. Atomic covalent-radius conventions enter only the very small activation in the two atomic comparisons. No cloud-number amplification is included. LUMI is retained qualitatively because no unique primary structural radius was fixed. The numbers reproduce the archived experiment-specific checks, not new fits to these experiments.

Appendix E. First-order Talbot design table

The following calculation uses the constants of Section 8 and the central LPF ceiling. The equality row is shown to three significant figures in physical discussion; additional numerical digits are retained here for reproduction.

Diameter (nm)	Mass (MDa)	Velocity ($\mathrm{m\,s^{-1}}$)	Total time (s)	$\mathcal{D}_D$	Drop (cm)
12	0.529069	41.9446	0.046907	0.014906	1.0789
14	0.840142	26.4141	0.074487	0.069440	2.7205
16	1.254090	17.6954	0.111187	0.262820	6.0618
18.30095	1.876678	11.8249	0.166386	1.0000	13.5745
20	2.449395	9.06003	0.217163	2.41163	23.1239
25	4.783974	4.63874	0.424146	21.6801	88.2106

Flux, velocity acceptance, optical response, thermal radiation, collisions and detection must still be propagated through a full conventional signal model. The table is a conditional design calculation, not evidence that an interference experiment at these settings has been achieved.

Appendix F. Mechanical cost beyond the Gaussian kernel

Consider a stationary compound-Poisson generator of the form (6), replacing μ_{r_d} by any normalized symmetric momentum-transfer measure μ. This generator belongs to the translation-covariant momentum-transfer class [27,28]. Assume a finite second moment and define the momentum-variance growth tensor

$$\mathsf{D}_{ij} = \Gamma \int d^3q\, \mu(\mathbf{q})\, q_i q_j. \tag{F1}$$

Symmetry gives zero mean force and a real attenuation rate

$$\mathcal{R}_\mu(\mathbf{d}) = \Gamma \int d^3q\, \mu(\mathbf{q}) \left[1 - \cos\left(\frac{\mathbf{q}\cdot\mathbf{d}}{\hbar}\right)\right] \le \frac{\mathbf{d}^{\mathsf{T}}\mathsf{D}\mathbf{d}}{2\hbar^2}. \tag{F2}$$

The inequality follows pointwise from $1-\cos u \le u^2/2$, before integration. For a prescribed path pair it yields

$$\mathcal{D}_\mu \le \frac{1}{2\hbar^2}\int_0^T dt\, \Delta\mathbf{x}(t)^{\mathsf{T}}\mathsf{D}\,\Delta\mathbf{x}(t). \tag{F3}$$

For an isotropic measure, $\mathsf{D} = D_C I$, recovering (33). The same second moment gives the free added covariance $\Delta\,\mathrm{Cov}\,\mathbf{X} = T^3\mathsf{D}/(3M^2)$, so (51) requires no Gaussian assumption. For anisotropic noise, a one-axis measurement constrains the appropriate projection rather than the entire tensor.

These are algebraic consequences of the stated class, not a microscopic derivation or a claim that all decoherence mechanisms have the same cost. Friction, memory, changing domains or system-dependent noise require their own evolution and response. The proof supplies the precise scope of the parameter-eliminated exclusion test.

Appendix G. Assumptions and status of the results

The effective theory uses a nonrelativistic centre-of-mass description of a fixed material domain, stationary parameters in a homogeneous patch, isotropic momentum transfer and a Gaussian resolving kernel. The hypotheses defining each theorem, the harmonic propagation and the phase-space approximation are stated in the corresponding sections. The following classification distinguishes mathematical consequences from physical identifications and completion tasks: **DERIVED** denotes a consequence of the displayed equations in their stated domain; **CONDITIONAL** a physical identification or extrapolation; **CALIBRATED** an input fixed by the stated experimental or diagnostic procedure; **OPEN** a construction still to be supplied; and **REJECTED** an inference excluded by the analysis.

Table 7: Assumptions and evidential status of the principal statements.

Statement	Status and requirement
Djamilars are the underlying geometric units	CONDITIONAL ontology; microscopic existence OPEN
Aperture-state law (2)	DERIVED from (1) at fixed density; kernel identification CONDITIONAL
Activation and bound-domain law (4)	CONDITIONAL structural postulates; microscopic derivation OPEN
Complete positivity, kernel, heating and moments	DERIVED for the specified fixed-domain generator
Size-independent reconstructed aperture	DERIVED for a nonzero fixed-aperture channel and a common domain prescription; Section 6.5
Exact CSL sphere comparison	DERIVED from the specified continuum mass-density kernel; plateau and noise must refer to the same channel; Appendix H
Unique size boundary and size slopes	DERIVED for the conditions of Proposition 1
Mechanical cost and localization-motion window	DERIVED within the stated kick class and declared requirements
Approximately classical motion	CONDITIONAL on preparation, coarse-graining, forces and noise tolerance
Physical individual outcomes	OPEN; (25)-(27) give a compatible conditional construction
Experimental and photophysical inputs	CALIBRATED as specified; radius and exponents are declared benchmarks
MUSCLE profile scale	CONDITIONAL diagnostic; numerical reproduction verified, absolute-fit deficiency unresolved
MUSCLE as a validated exclusion or detection	REJECTED for the present inference; adequate statistical model and coverage OPEN
LPF central ceiling	CONDITIONAL on the rigid-domain, independence and spectrum assumptions
Universal 25 nm critical radius	REJECTED as an inference from this dynamics
Guaranteed transition at 18.3 nm diameter	REJECTED; the calculated design intersection is CONDITIONAL
Common gravitational and stochastic origin	OPEN matching problem with CONDITIONAL cross-sector relations

The microscopic completion must determine the activation exponent and collective coupling, and supply a many-body rule for domain changes, arbitrarily weak binding and superposed internal structures. A shape-dependent mass-density coupling has a form factor and is not automatically the same channel as a Gaussian centre-of-mass kick acting on one whole domain. Transferring a prediction between experiments therefore retains the declared coupling and domain prescription.

Markovianity, isotropy and Gaussian transfer specify the effective realization. A spatially varying radius requires a completely positive inhomogeneous generator; simple substitution into (7) does not establish one. Prescribed positive time-dependent rates and radii in a homogeneous patch can define a completely positive time-local evolution, generally without time-homogeneous semigroup structure.

The displayed channel heats without friction. Dissipative or non-Markovian realizations have their own energy balance and spectral predictions. The gravitational completion must account for the compensating energy-momentum exchange. Electromagnetic radiation also requires the specified coupling: neutral rigid translation can suppress the leading electric dipole term, while internal, multipolar and retardation contributions require an electrodynamic calculation. No quantitative radiation-cancellation result is assumed in the present bounds.

Appendix H. Exact reconstructed length for a homogeneous CSL sphere

We compare the fixed-aperture channel with the continuum, mass-proportional, white-noise CSL centre-of-mass generator of a rigid body [8,25,26]. Adopt the momentum-transfer convention

$$w_C(\mathbf{q}) = \frac{\Lambda}{m_0^2}|\tilde{\rho}_m(\mathbf{q})|^2 e^{-r_C^2 q^2/\hbar^2}, \qquad \tilde{\rho}_m(\mathbf{q}) = \int d^3x\, \rho_m(\mathbf{x}) e^{-i\mathbf{q}\cdot\mathbf{x}/\hbar}. \tag{H1}$$

Here $r_C > 0$, $\Lambda > 0$, and m_0 fixes the reference-mass convention. The measure $w_C(\mathbf{q})d^3q$ has units of inverse time; for the conventional point-particle rate $\lambda(M/m_0)^2$, $\Lambda = \lambda r_C^3/(\pi^{3/2}\hbar^3)$. The body replaces $\Gamma_D\mu_{r_d}$ in (6) by w_C. For an isotropic body, define

$$\begin{aligned} \Gamma_C(d) &= \int d^3q\, w_C(\mathbf{q})[1-\cos(\mathbf{q}\cdot\mathbf{d}/\hbar)], \\ \Gamma_\infty &= \int d^3q\, w_C(\mathbf{q}), \qquad D = \frac{1}{3}\int d^3q\, q^2 w_C(\mathbf{q}). \end{aligned} \tag{H2}$$

Integrability gives the plateau by the Riemann-Lebesgue lemma, while the finite second moment gives $\Gamma_C''(0) = D/\hbar^2$. As in Section 3, D is the one-axis variance production, twice the Fokker-Planck diffusion coefficient. The ratio in (36) is defined for a nonzero channel. A bound on D and an unresolved plateau alone do not reconstruct this ratio.

For a homogeneous sphere of mass M and radius R, put $s = R/r_C$ and $x = qR/\hbar$. Its form factor is

$$\tilde{\rho}_m(\mathbf{q}) = M\frac{3j_1(x)}{x}, \qquad j_1(x) = \frac{\sin x - x\cos x}{x^2}. \tag{H3}$$

Direct evaluation yields the exact finite-radius expressions

$$\begin{aligned} \Gamma_\infty &= \frac{6\pi^2\Lambda\hbar^3M^2}{m_0^2R^3}\, g_{\mathrm{sph}}(s), \\ D &= \frac{3\pi^{3/2}\Lambda\hbar^5M^2}{m_0^2R^4r_C}\, h_{\mathrm{sph}}(s), \end{aligned} \tag{H4}$$

where

$$\begin{aligned} g_{\mathrm{sph}}(s) &= \mathrm{erf}(s) - \frac{3-e^{-s^2}}{\sqrt{\pi}\,s} + \frac{2(1-e^{-s^2})}{\sqrt{\pi}\,s^3}, \\ h_{\mathrm{sph}}(s) &= 1 - \frac{2}{s^2} + \left(1+\frac{2}{s^2}\right)e^{-s^2}. \end{aligned} \tag{H5}$$

To obtain the first expression, write the mass autocorrelation as the overlap volume of two spheres. At displacement $u \le 2R$ it is $\rho_m^2(4\pi R^3/3)[1-3u/(4R)+u^3/(16R^3)]$, and it vanishes for $u > 2R$.

Fourier transformation of the Gaussian in (H1), followed by $t = u/(2r_C)$, reduces the normalized integral to

$$g_{\rm sph}(s) = \frac{4}{\sqrt{\pi}} \int_0^s dt\, t^2 e^{-t^2} \left(1 - \frac{3t}{2s} + \frac{t^3}{2s^3}\right). \tag{H6}$$

Elementary Gaussian moments give (H5). For the diffusion integral, substitution of (H3) into (H2) gives $D = 12\pi\Lambda\hbar^5 M^2/(m_0^2 R^5)$ times the integral

$$\int_0^\infty dx\, x^2 j_1(x)^2 e^{-x^2/s^2} = \frac{\sqrt{\pi}\, s}{4}\, h_{\rm sph}(s). \tag{H7}$$

Expanding j_1, integrating its cross term by parts and using the Gaussian cosine integral gives this identity; the combined integrand is regular at the origin. Equations (H4)-(H7) also make the positive-integral origin of both shape functions explicit. Their direct closed forms lose numerical precision for very small s, where the verification script uses their convergent power series.

The normalization cancels exactly:

$$\boxed{r_{\rm eff}^2 = \sqrt{\pi}\, R r_C\, \frac{g_{\rm sph}(R/r_C)}{h_{\rm sph}(R/r_C)}.} \tag{H8}$$

The limiting expressions are

$$\begin{aligned} &g_{\rm sph}(s) = \frac{s^3}{6\sqrt{\pi}}[1 - 3s^2/10 + O(s^4)], \qquad h_{\rm sph}(s) = \frac{s^4}{6}[1 - s^2/2 + O(s^4)] \quad (s \ll 1), \\ &g_{\rm sph}(s) = 1 - \frac{3}{\sqrt{\pi}\, s} + O(s^{-3}), \qquad h_{\rm sph}(s) = 1 - \frac{2}{s^2} + O(e^{-s^2}) \qquad\qquad (s \gg 1). \end{aligned} \tag{H9}$$

Thus $r_{\rm eff}^2 = r_C^2[1 + s^2/5 + O(s^4)]$ for small spheres and $r_{\rm eff}^2 = \sqrt{\pi} R r_C[1 - 3/(\sqrt{\pi}s) + O(s^{-2})]$ for large spheres. At fixed material density and fixed CSL parameters, (H4) gives plateau slopes $6 \to 3$ and diffusion slopes $6 \to 2$. For the Djamilar law at fixed r_d, both moments instead carry the same factor $\Gamma_D(R)$ and their ratio gives r_d^2 exactly. This establishes the comparison in Section 6.5 within the two stated effective couplings.

Independent quadrature of the momentum-space form factor gives $r_{\rm eff}^2/r_C^2 = 1.0000200$ at $s = 0.01$. The ratios of (H8) to its leading large-radius expression are 0.9832721 at $s = 100$ and 0.9943802 at $s = 300$. The supplementary script reproduces these checks and the full crossover without a fitted normalization.

References

[1] A. Zerouta, *Gravity as Geometric Filtration: A Unified Framework for Cosmological and Quantum Phenomena*, Research Square preprint (2025). DOI: 10.21203/rs.3.rs-6570489/v1.

[2] A. Zerouta, *DJAMILAR: Gravity as Geometric Filtration — A Common Geometric Origin of Gravitation, Quantum-Classical Behaviour and Dark-Sector Phenomenology*, Research Square preprint, version 1 (2026). DOI: 10.21203/rs.3.rs-11144964/v1.

[3] H. D. Zeh, "On the interpretation of measurement in quantum theory," *Foundations of Physics* **1**, 69-76 (1970). DOI: 10.1007/BF00708656.

[4] E. Joos and H. D. Zeh, "The emergence of classical properties through interaction with the environment," *Zeitschrift für Physik B Condensed Matter* **59**, 223-243 (1985). DOI: 10.1007/BF01725541.

[5] W. H. Zurek, "Decoherence, einselection, and the quantum origins of the classical," *Reviews of Modern Physics* **75**, 715-775 (2003). DOI: 10.1103/RevModPhys.75.715.

[6] G. C. Ghirardi, A. Rimini and T. Weber, "Unified dynamics for microscopic and macroscopic systems," *Physical Review D* **34**, 470-491 (1986). DOI: 10.1103/PhysRevD.34.470.

[7] P. Pearle, "Combining stochastic dynamical state-vector reduction with spontaneous localization," *Physical Review A* **39**, 2277-2289 (1989). DOI: 10.1103/PhysRevA.39.2277.

[8] G. C. Ghirardi, P. Pearle and A. Rimini, "Markov processes in Hilbert space and continuous spontaneous localization of systems of identical particles," *Physical Review A* **42**, 78-89 (1990). DOI: 10.1103/PhysRevA.42.78.

[9] A. Bassi and G. Ghirardi, "Dynamical reduction models," *Physics Reports* **379**, 257-426 (2003). DOI: 10.1016/S0370-1573(03)00103-0.

[10] L. Diósi, "Models for universal reduction of macroscopic quantum fluctuations," *Physical Review A* **40**, 1165-1174 (1989). DOI: 10.1103/PhysRevA.40.1165.

[11] R. Penrose, "On Gravity's role in Quantum State Reduction," *General Relativity and Gravitation* **28**, 581-600 (1996). DOI: 10.1007/BF02105068.

[12] M. Arndt, O. Nairz, J. Vos-Andreae, C. Keller, G. van der Zouw and A. Zeilinger, "Wave-particle duality of C60 molecules," *Nature* **401**, 680-682 (1999). DOI: 10.1038/44348.

[13] S. Gerlich, S. Eibenberger, M. Tomandl et al., "Quantum interference of large organic molecules," *Nature Communications* **2**, 263 (2011). DOI: 10.1038/ncomms1263.

[14] S. Eibenberger, S. Gerlich, M. Arndt, M. Mayor and J. Tüxen, "Matter–wave interference of particles selected from a molecular library with masses exceeding 10 000 amu," *Physical Chemistry Chemical Physics* **15**, 14696-14700 (2013). DOI: 10.1039/C3CP51500A.

[15] Y. Y. Fein, P. Geyer, P. Zwick et al., "Quantum superposition of molecules beyond 25 kDa," *Nature Physics* **15**, 1242-1245 (2019). DOI: 10.1038/s41567-019-0663-9.

[16] A. Shayeghi, P. Rieser, G. Richter et al., "Matter-wave interference of a native polypeptide," *Nature Communications* **11**, 1447 (2020). DOI: 10.1038/s41467-020-15280-2.

[17] S. Pedalino, B. E. Ramírez-Galindo, R. Ferstl, K. Hornberger, M. Arndt and S. Gerlich, "Probing quantum mechanics with nanoparticle matter-wave interferometry," *Nature* **649**, 866-870 (2026). DOI: 10.1038/s41586-025-09917-9.

[18] K. Hornberger, S. Uttenthaler, B. Brezger, L. Hackermüller, M. Arndt and A. Zeilinger, "Collisional Decoherence Observed in Matter Wave Interferometry," *Physical Review Letters* **90**, 160401 (2003). DOI: 10.1103/PhysRevLett.90.160401.

[19] L. Hackermüller, K. Hornberger, B. Brezger, A. Zeilinger and M. Arndt, "Decoherence of matter waves by thermal emission of radiation," *Nature* **427**, 711-714 (2004). DOI: 10.1038/nature02276.

[20] K. Hornberger, J. E. Sipe and M. Arndt, "Theory of decoherence in a matter wave Talbot-Lau interferometer," *Physical Review A* **70**, 053608 (2004). DOI: 10.1103/PhysRevA.70.053608.

[21] K. Hornberger, "Thermal limitation of far-field matter-wave interference," *Physical Review A* **73**, 052102 (2006). DOI: 10.1103/PhysRevA.73.052102.

[22] G. Lindblad, "On the generators of quantum dynamical semigroups," *Communications in Mathematical Physics* **48**, 119-130 (1976). DOI: 10.1007/BF01608499.

[23] V. Gorini, A. Kossakowski and E. C. G. Sudarshan, "Completely positive dynamical semigroups of n-level systems," *Journal of Mathematical Physics* **17**, 821-825 (1976). DOI: 10.1063/1.522979.

[24] A. Bassi, K. Lochan, S. Satin, T. P. Singh and H. Ulbricht, "Models of wave-function collapse, underlying theories, and experimental tests," *Reviews of Modern Physics* **85**, 471-527 (2013). DOI: 10.1103/RevModPhys.85.471.

[25] L. Ferialdi and A. Bassi, "Continuous spontaneous localization reduction rate for rigid bodies," *Physical Review A* **102**, 042213 (2020). DOI: 10.1103/PhysRevA.102.042213.

[26] S. Nimmrichter, K. Hornberger and K. Hammerer, "Optomechanical Sensing of Spontaneous Wave-Function Collapse," *Physical Review Letters* **113**, 020405 (2014). DOI: 10.1103/PhysRevLett.113.020405.

[27] A. S. Holevo, "On translation-covariant quantum Markov equations," *Izvestiya: Mathematics* **59**, 427-443 (1995). DOI: 10.1070/IM1995v059n02ABEH000019.

[28] B. Vacchini, "Theory of Decoherence due to Scattering Events and Lévy Processes," *Physical Review Letters* **95**, 230402 (2005). DOI: 10.1103/PhysRevLett.95.230402.

[29] M. Toroš and A. Bassi, "Bounds on quantum collapse models from matter-wave interferometry: calculational details," *Journal of Physics A: Mathematical and Theoretical* **51**, 115302 (2018). DOI: 10.1088/1751-8121/aaabc6.

[30] S. Nimmrichter, K. Hornberger, P. Haslinger and M. Arndt, "Testing spontaneous localization theories with matter-wave interferometry," *Physical Review A* **83**, 043621 (2011). DOI: 10.1103/PhysRevA.83.043621.

[31] M. Schlosshauer, "Decoherence, the measurement problem, and interpretations of quantum mechanics," *Reviews of Modern Physics* **76**, 1267-1305 (2005). DOI: 10.1103/RevModPhys.76.1267.

[32] B. Schrinski, B. A. Stickler and K. Hornberger, "Collapse-induced orientational localization of rigid rotors," *Journal of the Optical Society of America B* **34**, C1-C7 (2017). DOI: 10.1364/JOSAB.34.0000C1.

[33] M. Bahrami, A. Smirne and A. Bassi, "Role of gravity in the collapse of a wave function: A probe into the Diósi-Penrose model," *Physical Review A* **90**, 062105 (2014). DOI: 10.1103/PhysRevA.90.062105.

[34] M. Armano, H. Audley, J. Baird et al., "Beyond the required LISA free-fall performance: New LISA Pathfinder results down to 20 microhertz," *Physical Review Letters* **120**, 061101 (2018), with the publisher's abstract correction of 21 February 2018. DOI: 10.1103/PhysRevLett.120.061101.

[35] M. Armano, H. Audley, J. Baird et al., "Calibrating the system dynamics of LISA Pathfinder," *Physical Review D* **97**, 122002 (2018). DOI: 10.1103/PhysRevD.97.122002.

[36] M. Armano et al., "In-depth analysis of LISA Pathfinder performance results: Time evolution, noise projection, physical models, and implications for LISA," *Physical Review D* **110**, 042004 (2024). DOI: 10.1103/PhysRevD.110.042004.

[37] B. Helou, B. J. J. Slagmolen, D. E. McClelland and Y. Chen, "LISA Pathfinder appreciably constrains collapse models," *Physical Review D* **95**, 084054 (2017). DOI: 10.1103/PhysRevD.95.084054.

[38] M. Carlesso, A. Bassi, P. Falferi and A. Vinante, "Experimental bounds on collapse models from gravitational wave detectors," *Physical Review D* **94**, 124036 (2016). DOI: 10.1103/PhysRevD.94.124036.

[39] S. Pedalino, B. E. Ramírez Galindo, R. Ferstl, K. Hornberger, M. Arndt and S. Gerlich, *Probing quantum mechanics with nanoparticle matter-wave interferometry - Dataset and code*, Zenodo (2025). DOI: 10.5281/zenodo.17502163.

[40] M. Carlesso, S. Donadi, L. Ferialdi, M. Paternostro, H. Ulbricht and A. Bassi, "Present status and future challenges of non-interferometric tests of collapse models," *Nature Physics* **18**, 243-250 (2022). DOI: 10.1038/s41567-021-01489-5.

[41] A. Vinante, R. Mezzena, P. Falferi, M. Carlesso and A. Bassi, "Improved Noninterferometric Test of Collapse Models Using Ultracold Cantilevers," *Physical Review Letters* **119**, 110401 (2017). DOI: 10.1103/PhysRevLett.119.110401.

[42] A. Vinante, M. Carlesso, A. Bassi et al., "Narrowing the Parameter Space of Collapse Models with Ultracold Layered Force Sensors," *Physical Review Letters* **125**, 100404 (2020). DOI: 10.1103/PhysRevLett.125.100404.

[43] S. Donadi, K. Piscicchia, R. Del Grande, C. Curceanu, M. Laubenstein and A. Bassi, "Novel CSL bounds from the noise-induced radiation emission from atoms," *The European Physical Journal C* **81**, 773 (2021). DOI: 10.1140/epjc/s10052-021-09556-0.

[44] S. Donadi, K. Piscicchia, C. Curceanu, L. Diósi, M. Laubenstein and A. Bassi, "Underground test of gravity-related wave function collapse," *Nature Physics* **17**, 74-78 (2021). DOI: 10.1038/s41567-020-1008-4.

[45] I. J. Arnquist, F. T. Avignone, A. S. Barabash et al., "Search for Spontaneous Radiation from Wave Function Collapse in the Majorana Demonstrator," *Physical Review Letters* **129**, 080401 (2022). DOI: 10.1103/PhysRevLett.129.080401. Erratum: *Physical Review Letters* **130**, 239902 (2023). DOI: 10.1103/PhysRevLett.130.239902.

[46] S. Nimmrichter and K. Hornberger, "Theory of near-field matter-wave interference beyond the eikonal approximation," *Physical Review A* **78**, 023612 (2008). DOI: 10.1103/PhysRevA.78.023612.

[47] S. L. Adler, "Lower and upper bounds on CSL parameters from latent image formation and IGM heating," *Journal of Physics A: Mathematical and Theoretical* **40**, 2935-2957 (2007). DOI: 10.1088/1751-8113/40/12/S03. Erratum: *Journal of Physics A: Mathematical and Theoretical* **40**, 13501 (2007). DOI: 10.1088/1751-8121/40/44/C01.

[48] L. Figurato, M. Dirindin, J. L. Gaona-Reyes, M. Carlesso, A. Bassi and S. Donadi, "On the effectiveness of the collapse in the Diósi–Penrose model," *New Journal of Physics* **26**, 113004 (2024). DOI: 10.1088/1367-2630/ad8c77.

[49] R. P. Feynman and F. L. Vernon, Jr., "The theory of a general quantum system interacting with a linear dissipative system," *Annals of Physics* **24**, 118-173 (1963). DOI: 10.1016/0003-4916(63)90068-X.

[50] B. L. Hu and E. Verdaguer, "Stochastic gravity: Theory and applications," *Living Reviews in Relativity* **11**, 3 (2008). DOI: 10.12942/lrr-2008-3.

[51] S. Nimmrichter and K. Hornberger, "Macroscopicity of mechanical quantum superposition states," *Physical Review Letters* **110**, 160403 (2013). DOI: 10.1103/PhysRevLett.110.160403.

[52] G. Cowan, K. Cranmer, E. Gross and O. Vitells, "Asymptotic formulae for likelihood-based tests of new physics," *European Physical Journal C* **71**, 1554 (2011). DOI: 10.1140/epjc/s10052-011-1554-0. Erratum: *The European Physical Journal C* **73**, 2501 (2013). DOI: 10.1140/epjc/s10052-013-2501-z.

[53] H. E. Sauceda, J. J. Pelayo, F. Salazar, L. A. Pérez and I. L. Garzón, "Vibrational spectrum, caloric curve, low-temperature heat capacity, and Debye temperature of sodium clusters: The Na139+ case," *Journal of Physical Chemistry C* **117**, 11393-11398 (2013). DOI: 10.1021/jp401903f.

[54] A. Aguado, J. M. López, J. A. Alonso and M. J. Stott, "Melting in large sodium clusters: An orbital-free molecular dynamics study," *Journal of Physical Chemistry B* **105**, 2386-2392 (2001). DOI: 10.1021/jp0018504.

[55] M. Schmidt, R. Kusche, T. Hippler et al., "Negative heat capacity for a cluster of 147 sodium atoms," *Physical Review Letters* **86**, 1191-1194 (2001). DOI: 10.1103/PhysRevLett.86.1191.

[56] M. Schmidt, T. Hippler, J. Donges et al., "Caloric curve across the liquid-to-gas change for sodium clusters," *Physical Review Letters* **87**, 203402 (2001). DOI: 10.1103/PhysRevLett.87.203402.

[57] C. Hock, M. Schmidt and B. von Issendorff, "Low-temperature caloric behavior of a free sodium nanoparticle," *Physical Review B* **84**, 113401 (2011). DOI: 10.1103/PhysRevB.84.113401.

[58] S. Liu, Y.-J. Lu, M. M. Kappes and J. A. Ibers, "The structure of the C60 molecule: X-ray crystal structure determination of a twin at 110 K," *Science* **254**, 408-410 (1991). DOI: 10.1126/science.254.5030.408.

[59] J. Williams et al., "Pathfinder experiments with atom interferometry in the Cold Atom Lab onboard the International Space Station," *Nature Communications* **15**, 6414 (2024). DOI: 10.1038/s41467-024-50585-6.

[60] A. Peters, K. Y. Chung and S. Chu, "Measurement of gravitational acceleration by dropping atoms," *Nature* **400**, 849-852 (1999). DOI: 10.1038/23655.